The Zwicky Transient Facility Bright Transient Survey. I. Spectroscopic Classification and the Redshift Completeness of Local Galaxy Catalogs

C. Fremling[1] , A. A. Miller[2,3] , Y. Sharma[1] , A. Dugas[1,4] , D. A. Perley[5] , K. Taggart[5] , J. Sollerman[6] , A. Goobar[7] ,
M. L. Graham[8] , J. D. Neill[1] , J. Nordin[9] , M. Rigault[10] , R. Walters[1,11] , I. Andreoni[1] , A. Bagdasaryan[1] , J. Belicki[11] ,
C. Cannella[12] , E. C. Bellm[8] , S. B. Cenko[13] , K. De[1] , R. Dekany[11] , S. Frederick[14] , V. Z. Golkhou[8,15,21] ,
M. J. Graham[1] , G. Helou[16] , A. Y. Q. Ho[1] , M. M. Kasliwal[1] , T. Kupfer[17] , R. R. Laher[16] , A. Mahabal[1,18] ,
F. J. Masci[16] , R. Riddle[11] , B. Rusholme[16] , S. Schulze[19] , D. L. Shupe[16] , R. M. Smith[11] , S. van Velzen[14,20] ,
Lin Yan[11] , Y. Yao[1] , Z. Zhuang[1] , and S. R. Kulkarni[1]

[1] Division of Physics, Mathematics and Astronomy, California Institute of Technology, Pasadena, CA 91125, USA; fremling@caltech.edu
[2] Center for Interdisciplinary Exploration and Research in Astrophysics and Department of Physics and Astronomy, Northwestern University, 1800 Sherman Avenue,
Evanston, IL 60201, USA
[3] The Adler Planetarium, Chicago, IL 60605, USA
[4] Institute for Astronomy, University of Hawai'i, 2680 Woodlawn Drive, Honolulu, HI 96822, USA
[5] Astrophysics Research Institute, Liverpool John Moores University, Liverpool Science Park, 146 Brownlow Hill, Liverpool L35RF, UK
[6] Department of Astronomy, The Oskar Klein Center, Stockholm University, AlbaNova, SE-10691 Stockholm, Sweden
[7] Department of Physics, The Oskar Klein Center, Stockholm University, AlbaNova, SE-10691 Stockholm, Sweden
[8] DIRAC Institute, Department of Astronomy, University of Washington, 3910 15th Avenue NE, Seattle, WA 98195, USA
[9] Institut fur Physik, Humboldt-Universitat zu Berlin, Newtonstr. 15, D-12489, Berlin, Germany
[10] Université Clermont Auvergne, CNRS/IN2P3, Laboratoire de Physique de Clermont, F-63000 Clermont-Ferrand, France
[11] Caltech Optical Observatories, California Institute of Technology, Pasadena, CA 91125, USA
[12] Department of Electrical and Computer Engineering, Duke University, Durham, NC 27708, USA
[13] Astrophysics Science Division, NASA Goddard Space Flight Center, 8800 Greenbelt Road, Greenbelt, MD 20771, USA
[14] Department of Astronomy, University of Maryland, College Park, MD 20742, USA
[15] The eScience Institute, University of Washington, Seattle, WA 98195, USA
[16] IPAC, California Institute of Technology, 1200 E. California Boulevard, Pasadena, CA 91125, USA
[17] Kavli Institute for Theoretical Physics, University of California, Santa Barbara, CA 93106, USA
[18] Center for Data Driven Discovery, California Institute of Technology, Pasadena, CA 91125, USA
[19] Benoziyo Center for Astrophysics, The Weizmann Institute of Science, Rehovot 76100, Israel
[20] Center for Cosmology and Particle Physics, New York University, NY 10003, USA

Abstract

The Zwicky Transient Facility (ZTF) is performing a three-day cadence survey of the visible northern sky ($\sim 3\pi$) with newly found transient candidates announced via public alerts. The ZTF Bright Transient Survey (BTS) is a large spectroscopic campaign to complement the photometric survey. BTS endeavors to spectroscopically classify all extragalactic transients with $m_{peak} \leqslant 18.5$ mag in either the g_{ZTF} or r_{ZTF} filters, and publicly announce said classifications. BTS discoveries are predominantly supernovae (SNe), making this the largest flux-limited SN survey to date. Here we present a catalog of 761 SNe, classified during the first nine months of ZTF (2018 April 1–2018 December 31). We report BTS SN redshifts from SN template matching and spectroscopic host-galaxy redshifts when available. We analyze the redshift completeness of local galaxy catalogs, the redshift completeness fraction (RCF; the ratio of SN host galaxies with known spectroscopic redshift prior to SN discovery to the total number of SN hosts). Of the 512 host galaxies with SNe Ia, 227 had previously known spectroscopic redshifts, yielding an RCF estimate of 44% ± 4%. The RCF decreases with increasing distance and decreasing galaxy luminosity (for $z < 0.05$, or ~ 200 Mpc, RCF ≈ 0.6). Prospects for dramatically increasing the RCF are limited to new multifiber spectroscopic instruments or wide-field narrowband surveys. Existing galaxy redshift catalogs are only $\sim 50\%$ complete at $r \approx 16.9$ mag. Pushing this limit several magnitudes deeper will pay huge dividends when searching for electromagnetic counterparts to gravitational wave events or sources of ultra-high-energy cosmic rays or neutrinos.

Unified Astronomy Thesaurus concepts: Supernovae (1668); Galaxies (573); Redshift surveys (1378);
Surveys (1671)

Supporting material: data behind figures, machine-readable tables

1. Introduction

Fritz Zwicky and Walter Baade first hypothesized that supernovae (SNe) were the transition of normal stars into neutron stars (Baade & Zwicky 1934). To test this hypothesis, Zwicky used the 18 inch Schimdt telescope commissioned on Palomar mountain in 1936 to carry out the first systematic SN survey (Zwicky 1938a, 1938b, 1942). This survey was carried out by visually inspecting photographic plates of nebulae[22] and identifying new point sources. Twelve SNe were identified by Zwicky between 1936 September 5 and 1940 January 1.

Since the pioneering efforts by Zwicky, a variety of SN types have been identified through spectroscopy (see, e.g., Filippenko 1997). Thermonuclear SNe (SNe Ia) in particular

---

[21] Moore-Sloan, WRF Innovation in Data Science, and DIRAC Fellow.

[22] At the time, the term nebulae encompassed any diffuse astronomical object, including galaxies.

have proven to be invaluable tools to measure cosmological distances (e.g., Goobar & Leibundgut 2011), and the study of SNe Ia eventually led to the remarkable discovery of the accelerating expansion of the universe (Riess et al. 1998; Perlmutter et al. 1999). Studies of core-collapse (CC) SNe have led to considerable insights into massive star evolution: extragalactic neutrinos were detected in SN 1987A (Hirata et al. 1987), a γ-ray burst was associated with SN 1998bw (Galama et al. 1998), and direct evidence for binary-star-driven mass loss was seen in SN 1993J (e.g., Schmidt et al. 1993; Fox et al. 2014).

In order to constrain cosmological models and to characterize both SNe in general and the various SN types and their host galaxies, a large number of SN surveys have been carried out since Zwicky's time. The scope of these surveys largely traces the progress made in both automation and detector technology during the last few decades. The first systematic search for SNe using a charge-coupled device (CCD) was performed on the 1.5 m telescope at La Silla (Norgaard-Nielsen et al. 1989). The field of view (FoV) of this telescope and CCD was $2.'5 \times 4'$, and the survey was designed to find a thermonuclear SN at high redshift. Two SNe, one SN Ia and one probable SN II, were found in two years. More recent examples of SN surveys that have also been able to systematically classify their SN candidates using spectroscopy include, for example, the Lick Observatory Supernova Search (LOSS; Li et al. 2000), the Nearby Supernova Factory (SNfactory; Aldering et al. 2002), the Sloan Digital Sky Survey-II (SDSS-II) SN Survey (Frieman et al. 2008), and the Supernova Legacy Survey (SNLS; Astier et al. 2006). In the last few years, based on statistics on the Transient Name Server (TNS[23]), several surveys have been discovering hundreds of SNe that are also being spectroscopically classified, including the Palomar Transient Factory (PTF; Law et al. 2009), the Asteroid Terrestrial-impact Last Alert System (ATLAS; Tonry et al. 2018), the All-Sky Automated Survey for SuperNovae (ASAS-SN; Shappee et al. 2014), and the Panoramic Survey Telescope and Rapid Response System (Pan-STARRS1, hereafter PS1; Chambers et al. 2016) Medium Deep Survey.

The past few decades have seen a growing complexity in SN search surveys, with the general trend being an increase in volumetric survey speed (e.g., Bellm 2016) and consequently the number of SN discoveries. Given the scarcity of spectroscopic resources for SN follow-up observations, the increase in SN discoveries has resulted in a smaller fraction of the SNe being classified over time. Of the ongoing surveys, only ASAS-SN is able to maintain close to complete spectroscopic coverage (95% ± 3% for $m_{\mathrm{peak}} < 16.5$; Holoien et al. 2019), largely because ASAS-SN only detects very bright SNe. Otherwise, the typical strategies are to either (i) focus entirely on the most nearby galaxies (LOSS employed this strategy and maintained a nearly complete survey for ~10 yr), (ii) focus observations on likely SNe Ia to study cosmology (e.g., SDSS-II, SNLS), or (iii) target only a subset of SN candidates (e.g., PTF, ATLAS). Any of these choices result in major systematic ambiguities underlying any attempt to derive SN rates and demographics, or to use SNe from these surveys as population probes of galaxies. Nevertheless, these compromises have been necessary given the resources on hand.

With the Zwicky Transient Facility (ZTF; Bellm et al. 2019a, 2019b; Graham et al. 2019; Dekany et al. 2020) in combination with the fully automated Spectral Energy Distribution Machine (SEDM; Ben-Ami et al. 2012; Blagorodnova et al. 2018; Rigault et al. 2019), a low-resolution ($R \sim 100$), integral-field-unit (IFU) spectrograph mounted on the robotic Palomar 60 inch telescope (P60; Cenko et al. 2006), we have set out to address the lack of spectroscopic completeness described above. We aim to monitor the entire visible sky at moderate cadence while being complete in terms of spectroscopic classification. The 47 deg^2 FoV of the ZTF camera, along with upgrades to the Palomar 48 inch (P48) telescope and dome, achieves a survey speed of 3750 deg^2 hr^{-1}, to a 5σ depth of ~20.5 mag in r_{ZTF} using 30 s exposures. This allows most of the sky visible from Palomar to be imaged at a 3 day cadence (see Section 2 for details). Furthermore, SEDM is capable of classifying >10 SNe in the 18.5–19 mag range every night. A significant amount of time is also allocated to this project on the Palomar 200 inch telescope (P200), Keck I, the Liverpool Telescope (LT), Apache Point Observatory (APO), and the Nordic Optical Telescope (NOT). These resources are used to supplement our SEDM observations when SEDM classification is not possible, and the combination enables the ZTF Bright Transient Survey (BTS): an SN survey of unprecedented scale and spectroscopic completeness in the local universe.

The primary goal of the BTS is to spectroscopically classify and publicly report every extragalactic transient with g_{peak} or $r_{\mathrm{peak}} < 18.5$ mag in the northern sky covered by the public ZTF surveys.[24] This effort has produced the first large, magnitude-complete sample of transients to g_{peak} or $r_{\mathrm{peak}} < 18.5$ mag.[25] In this paper, we will focus on SNe, but the BTS also finds and classifies tidal disruption events (TDEs), which will be analyzed separately, and other extragalactic phenomena such as massive active galactic nucleus (AGN) flares, and fast and highly energetic transients such as AT 2018cow[26] (Prentice et al. 2018; Ho et al. 2019; Perley et al. 2019), whose nature remains mysterious. Here, we present a catalog of the 761 BTS SNe classified during the first 9 months of the survey (2018 April 1–2018 December 31; Table 1). Our catalog contains redshifts based on SN template matching (Blondin & Tonry 2007) and spectroscopic host-galaxy redshifts when available. For the host galaxies, we also provide mid-infrared (mid-IR) flux measurements from the Wide-field Infrared Survey Explorer (WISE; Wright et al. 2010) and optical/near-infrared flux measurements from the Panoramic Survey Telescope and Rapid Response System (PS1; Chambers et al. 2016).

We expect that this sample, and its ongoing extension through 2019 and 2020, will be useful for a wide variety of topics within SN astrophysics, some of which will be the focus of follow-up papers. In this paper, we focus on an analysis of the redshift completeness of local galaxy catalogs (Section 5), dubbed as the Redshift Completeness Fraction (RCF; the number of SN host galaxies with known redshift prior to SN discovery divided by the total number of SNe). The methodology for this analysis closely follows that of Kulkarni et al. (2018). Alongside this paper, we have released our open-source analysis of the RCF at https://github.com/adamamiller/bright_transient_survey.

---

[23] https://wis-tns.weizmann.ac.il/stats-maps

[24] Excluding the galactic plane ($\pm 7°$).
[25] The saturation limit of ZTF is ~14 mag.
[26] The internal ZTF designation for AT 2018cow is ZTF18abcfcoo.

Table 1
ZTF BTS SNe

ZTF Name	α_{SN} (J2000.0)	δ_{SN} (J2000.0)	IAU Name	TNS Internal Name	Discovered by	$E(B-V)$[b] (mag)	SN Type	z_{SN}[c]	Observed Time and Magnitude at Maximum Brightness[a]					
									t_g (JD′)[d]	m_g (mag)	σ_{m_g} (mag)	t_r (JD′)[d]	m_r (mag)	σ_{m_r} (mag)
ZTF18aabssth	11:00:45.38	+22:17:15.0	SN 2018aex	ZTF18aabssth	ZTF	0.015	II	0.026	494.05	20.44	0.19	218.71	18.74	0.05
ZTF18aabxlsv	10:29:51.62	+09:00:46.6	SN 2018aks	ASASSN-18ga	ASAS-SN	0.025	Ib	0.055	605.71	20.33	0.19	224.68	18.64	0.04
ZTF18aaemivw	10:33:42.69	+39:29:26.6	SN 2018hus	ZTF18aaemivw	ZTF	0.012	Ia	0.065	423.96	19.00	0.16	534.87	17.95	0.15
ZTF18aagpzjk	07:59:25.01	+16:25:34.5	SN 2018afm	⋯	POSS	0.031	II	0.013	⋯	⋯	⋯	217.66	17.46	0.02
ZTF18aagrdcs	14:33:19.98	+41:16:02.3	SN 2018alc	ASASSN-18ge	ASAS-SN	0.012	Ib	0.024	547.91	17.37	0.05	217.90	16.67	0.01
ZTF18aagrtxs	13:14:25.46	+50:58:39.7	SN 2018amo	ASASSN-18gi	ASAS-SN	0.010	Ia	0.018	214.76	16.52	0.02	214.73	16.46	0.02
ZTF18aagstdc	15:50:03.56	+42:05:18.5	SN 2018apn	ASASSN-18gs	ASAS-SN	0.018	Ia	0.038	210.86	17.24	0.02	539.01	17.27	0.06
ZTF18aagtcxj	16:32:11.55	+42:42:48.3	SN 2018aqm	⋯	TNTS	0.011	Ia	0.033	539.03	19.01	0.19	219.96	18.09	0.03
ZTF18aahesrp	08:35:45.43	+28:16:12.9	SN 2018aqy	ATLAS18mzs	ATLAS	0.036	Ia	0.051	⋯	⋯	⋯	217.69	18.54	0.07
ZTF18aahfeiy	10:17:15.57	+43:31:24.2	SN 2018loy	ZTF18aahfeiy	ZTF	0.010	Ia	0.071	429.99	20.53	0.21	214.71	18.15	0.05
ZTF18aahfgyz	11:41:07.99	+24:49:10.4	SN 2018ast	⋯	Y. Tanaka	0.023	Ia-91bg	0.011	487.04	20.04	0.16	218.80	16.46	0.01
ZTF18aahfqbc	12:10:38.22	+39:23:47.8	SN 2018aoq	kait-18P	LOSS	0.023	II	0.001	538.82	16.45	0.07	214.73	15.40	0.01
ZTF18aahfxnn	11:46:11.96	+09:21:18.0	SN 2018bau	ZTF18aahfxnn	ZTF	0.026	Ia	0.074	⋯	⋯	⋯	227.75	18.61	0.03
ZTF18aahfzea	12:05:26.66	+20:17:56.8	SN 2018aqh	ATLAS18myy	ATLAS	0.033	Ia	0.025	594.69	19.68	0.19	217.76	16.31	0.01
ZTF18aahheaj	13:00:26.51	+18:37:09.8	SN 2018avp	ASASSN-18ii	ASAS-SN	0.022	Ia	0.047	⋯	⋯	⋯	227.77	17.87	0.03
ZTF18aahhenr	13:49:27.17	+26:27:43.6	SN 2018are	ASASSN-18hh	ASAS-SN	0.010	Ia-91T	0.078	⋯	⋯	⋯	222.78	18.30	0.03
ZTF18aahhqih	09:14:55.22	+46:54:08.8	SN 2018amb	⋯	G. Cortini	0.016	II	0.021	522.90	19.45	0.11	257.72	17.77	0.04
ZTF18aahhzqn	11:55:01.16	+32:04:31.3	SN 2018avy	Gaia18aze	Gaia	0.020	Ib/c	0.034	472.01	20.36	0.20	221.75	18.14	0.04
ZTF18aahjafd	13:13:05.87	+23:27:33.6	SN 2018loz	ZTF18aahjafd	ZTF	0.010	Ia	0.044	575.80	18.52	0.08	230.73	17.38	0.09
ZTF18aahmhxu	11:47:04.08	+19:33:02.9	SN 2018atq	⋯	TNTS	0.027	SLSN-II	0.167	575.77	19.44	0.10	266.73	18.43	0.08

Notes. References for SNe that were recovered by ZTF and discovered elsewhere ("Discovered by" in the table) are as follows: ASAS-SN (Shappee et al. 2014); ATLAS (Tonry et al. 2018); the Corona Borealis Observatory Supernova Survey (CSNS; Sun et al. 2018); G. Cortini (2018); DLT40 (Tartaglia et al. 2018); Gaia (Hodgkin et al. 2013); K. Itagaki (2018a, 2018b); the Italian Supernovae Search Project (ISSP; http://italiansupernovae.org/); LOSS (Filippenko et al. 2001); the Mobile Astronomical System of TElescope Robots (MASTER; Gorbovskoy et al. 2013); the Puckett Observatory Supernova Search (POSS; http://www.posssupernova.com/); PS1 (Chambers et al. 2016); J. Grzegorzek (2018); the PMO-Tsinghua Supernova Survey (PTSS); the Great Supernova Hunt (SNhunt; http://nesssi.cacr.caltech.edu/SNhunt/); the Tsinghua University-National Astronomical Observatories, Chinese Academy of Sciences Transient Survey (TNTS; Zhang et al. 2015); the Xinming Observatory Supernova Survey (XOSS; Zhang et al. 2018); and Y. Tanaka (2018).
[a] Time and magnitude of maximum brightness are determined directly from the observations, as available in the AVRO alert packets. "⋯" is used when the SN was not detected in either the g_{ZTF} or r_{ZTF} filter. No correction for extinction has been applied.
[b] $E(B-V)$ is determined using the Schlafly & Finkbeiner (2011) updates to the Schlegel et al. (1998) maps.
[c] Determined from SNID (see text). No corrections for heliocentric, galactocentric, or host-galaxy rotation velocity are applied to z_{SN}.
[d] JD′ = JD-2458,000.

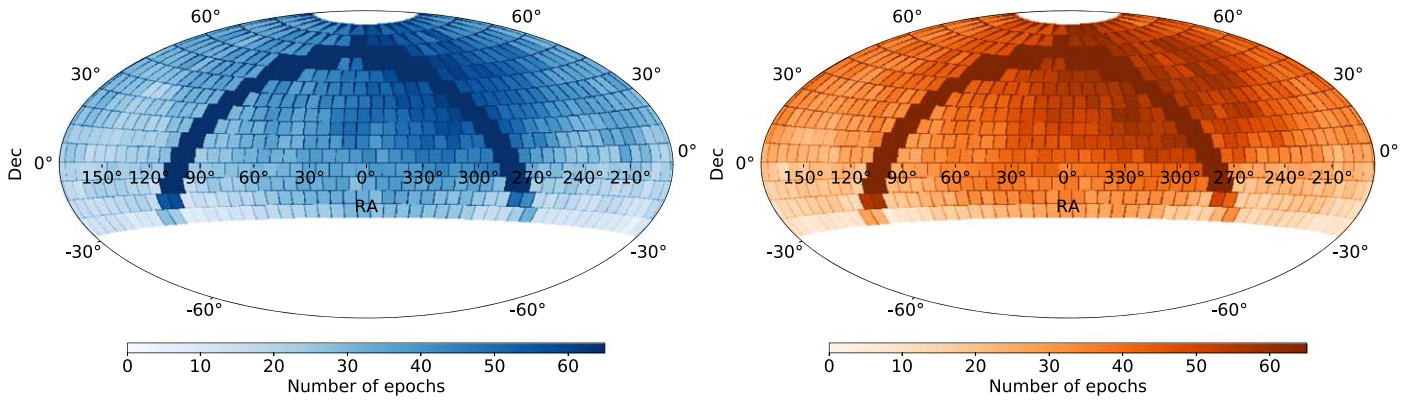(This table is available in its entirety in machine-readable form.)

Figure 1. Coverage maps for the ZTF MSIP surveys, in the g_{ZTF} (left panel) and r_{ZTF} bands (right panel) between 2018 April 1 and 2018 December 31. The colored rectangles represent the fixed ZTF main field grid. The color intensity indicates the number of observations during this time period, truncated to a maximum of 65.

2. Survey Design

Transient candidates for the BTS are provided by the public ZTF surveys: the Northern Sky Survey (NSS) and the Galactic Plane Survey (GPS). These surveys are made possible by an award from the NSF Mid-Scale Innovations Program (MSIP), and we henceforth refer to them as the ZTF MSIP surveys (see Bellm et al. 2019a for details). The NSS covers $\approx 13{,}000\,\mathrm{deg}^2$ of the northern sky at a 3 day cadence in the g_{ZTF} and r_{ZTF} filters, while using 34% of the P48 telescope time. The GPS covers $\approx 1500\,\mathrm{deg}^2$ of the galactic plane at a 1 day cadence, also in the g_{ZTF} and r_{ZTF} filters, and uses 6% of the P48 telescope time.

The BTS avoids low Galactic latitudes by design; we reject all transient candidates found within $7°$ of the Galactic plane (see Section 2.1). The combination of significant Galactic extinction and the BTS Galactic plane cut means that the vast majority of the transients in the BTS originate from the NSS. However, due to the large FoV and the fixed main field grid used by ZTF (Masci et al. 2019), some of the GPS fields still allow transients to be found and monitored after a $7°$ galactic plane cut. During 2018, we classified two SNe within GPS fields.

The images from the ZTF MSIP surveys are processed and analyzed at IPAC by an automated pipeline (Masci et al. 2019) that uses the Zackay et al. (2016) difference-imaging method. The pipeline produces transient alert packets from the difference images in the Apache Avro^TM format.[27] The Avro alert packets are distributed through the University of Washington (UW) as a Kafka data stream.[28] The alert stream originating from the ZTF MSIP surveys is the data source for BTS transient candidates. The full ZTF Alert Distribution System (ZADS) is described in detail in Patterson et al. (2019).

Figure 1 shows the g_{ZTF}- and r_{ZTF}-band coverage maps of the ZTF MSIP surveys, between 2018 April 1 and 2018 December 31. The distribution of revisit times (cadence) for the NSS for each field during the same time period, excluding 2018 September 29–2018 October 31 when the P48 was undergoing maintenance, is shown in Figure 2. Approximately 70% of the NSS observations were carried out at the planned 3 day cadence, and ~90% of revisits occurred within ≤6 days during 2018. For the GPS, around 80% of the observations were
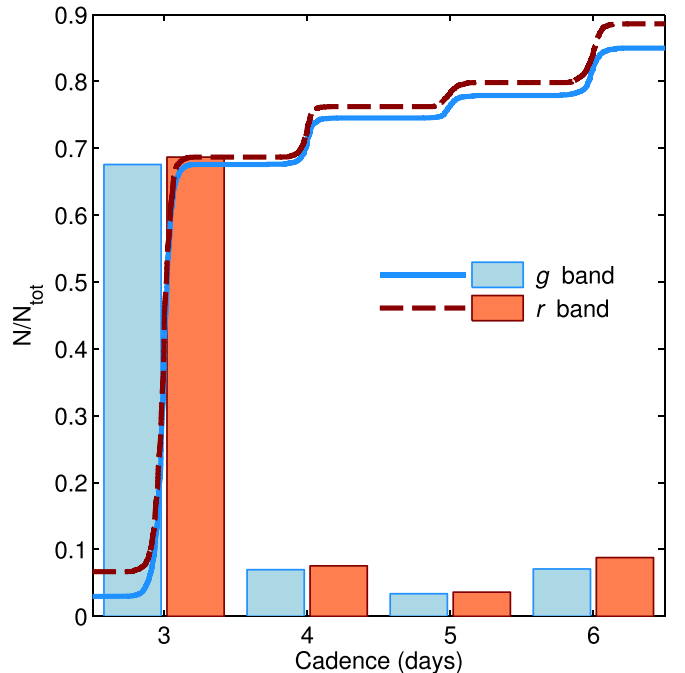

Figure 2. Cadence distribution for the ZTF NSS, in the g_{ZTF} (blue bars) and r_{ZTF} bands (red bars), truncated at six days. Cumulative distributions are shown as a blue solid line for the g band and a red dashed line for the r band. N/N_{tot} is the fraction of observations at a specific cadence compared to the total number of observations between 2018 April 1 and 2018 December 31.

carried out at a 1 day cadence. However, because only two BTS SNe were found and classified during 2018 in the GPS fields, the GPS cadence is not representative for the BTS.

In order to identify bright SN candidates within the raw ZTF alert stream produced by the MSIP surveys, we utilize the filtering capability within the GROWTH Marshal (Kasliwal et al. 2019) to apply the candidate filter described below (Section 2.1). The GROWTH Marshal framework is also used to organize BTS sources and the corresponding spectroscopic follow-up efforts (Sections 2.2, 2.3).

2.1. Supernova Candidate Filter

The BTS filter used between 2018 April 1st and 2018 December 31st was deliberately designed to be simple, in order to minimize the risk of false negatives (i.e., real transients that

---

are not saved as part of the program). Using the GROWTH `Marshal` alert filtering system, we applied the following cuts to the raw ZTF alert stream in order to identify bright SN candidates:

1. Alerts at low Galactic latitudes ($|b| \leqslant 7°$) are rejected.
2. Alerts with a random-forest-based machine-learning real-bogus score (`rbscore`; Mahabal et al. 2019) of less than 0.2 are rejected. This choice results in a completeness (i.e., 1—false negative rate) of >99% (Figure 16 in Duev et al. 2019).
3. Alerts produced at the position of known stars, as identified in the catalog created by Tachibana & Miller (2018), are rejected. A small fraction of galaxies (estimated to be <0.5% in Tachibana & Miller 2018), and thus nuclear SNe, will be missed as a result of this cut.
4. Alerts produced close to very bright stars have been rejected (<20″ for <15 mag stars; ∼1% loss of survey area[29]).
5. Alerts that do not include at least two detections separated by a minimum of 30 minutes are rejected (moving object filter).
6. Alerts with negative flux relative to the reference image are rejected.
7. The alert must include at least one epoch with $m < 19$ mag (in the g_{ZTF} or r_{ZTF} band), otherwise it is rejected.

The BTS filter effectively passes all alerts brighter than 19 mag that are not consistent with stellar events (star detected in PS1) or moving objects for human vetting (scanning; Section 2.2).

2.2. Human Candidate Vetting

On a typical night in 2018, a few hundred alerts passed the BTS filter. These BTS transient candidates were visually inspected by a team of scanners on a daily basis. To organize this effort, we use the GROWTH `Marshal` (Kasliwal et al. 2019), where the lightcurves and image cutouts (science, reference, and subtraction) contained in the Avro packets of the passing alerts are collected on a scanning page for each night. Supplementary information is also displayed, such as PS1 and SDSS color composite cutouts centered on the position of the transient; the star–galaxy separation score (`sgscore`), which gives a probability that the closest PS1 counterpart is an extended galaxy or a point-like star (Tachibana & Miller 2018); multiband photometry of this PS1 counterpart, a cross-check for known near earth objects (NEOs); and information about if and when there have been previous ZTF alerts at the same position that are not part of the 30 day history contained in the alert packet itself. External catalog cross-matches (e.g., NED, TNS, SIMBAD, VizieR) are also linked through the GROWTH `Marshal` to provide additional contextual information for each potential SN candidate.

The human-vetting process essentially consisted of inspecting the information contained in the Avro packets for each alert that passed our filter and also taking into account any relevant supplementary information available in order to rule out variability from a stellar counterpart, and to reject alerts produced by known AGNs.

Among the passing alerts, 5–15 SN candidates are typically identified by the human scanners as good SN candidates and assigned for spectroscopic follow-up, per night.[30] The two main contaminants in our scanning process are cataclysmic variables (CVs) that are too faint to be seen in PS1 in their quiescent phase, and therefore lack an `sgscore`, and AGNs. Both of these must be avoided, given our limited spectroscopic resources. We have found that the vast majority of CVs can be avoided by monitoring the lightcurve behavior until ∼1 week after the initial outburst and comparing the evolution with typical CV lightcurves.[31] This is especially effective as ZTF produces both g_{ZTF}- and r_{ZTF}-band photometry for virtually all transients that are detected.

Filtering AGNs is more challenging: excluding all AGNs from the BTS could inadvertently reject an SN that has exploded near the nucleus of a galaxy that harbors an AGN. Filtering on past variability is a very effective way of excluding AGNs, but for the sample presented here, the baseline of ZTF observations was only a few weeks or months, which is not always a sufficient amount of time for the AGN to change in flux enough to be recognized as a variable object. We have generally not triggered spectroscopic follow-up for alerts that are positionally coincident with known AGNs (e.g., the ALLWISE mid-IR AGN catalog, Secrest et al. 2015; the Million Quasar catalog, Flesch 2015), unless the photometric evolution of the transient is very similar to that of an SN. Thus, the BTS is incomplete for SNe near AGNs (a focused survey with the specific goal of discovering SNe in galaxies with an AGN is needed to address this).

2.2.1. Completeness of the BTS Filter

To assess the completeness of our BTS GROWTH `Marshal` filter (Section 2.1) and human-scanning effort (Section 2.2), we have reprocessed and refiltered all public ZTF alerts between 2018 April 1 and 2018 December 31 using the `AMPEL` system (Soumagnac & Ofek 2018; Nordin et al. 2019). Two filters were applied for this exercise: a variant of our BTS GROWTH `Marshal` filter converted to work within `AMPEL`[32] and the `AMPEL` TNS channel filter described in Nordin et al. (2019).

After the filtering step, we combined the passing candidates from both filters and imposed a cut requiring at least five detections, a peak brightness <18.5 mag,[33] no more than one negative detection, and a time between the first and last detection more than 5 days and less than 90 days.[34] Finally, we also required that the candidate pass a version of the GROWTH `Marshal` filter that checks all associated Avro packets for that candidate. All of the remaining objects that were not saved on the GROWTH `Marshal` were then vetted individually to

---

[29] Based on randomly injecting 10,000 SNe within the survey footprint and matching against PS1 stars.

[30] This number strongly depends on the weather; after a period of bad weather, a large number of SNe will be recovered when observations are resumed. Good weather periods produce a more constant number each night.

[31] CVs feature a fast evolution (rise time of ∼1–2 days, decline of ∼7–10 days), and their $g_{ZTF} - r_{ZTF}$ colors are persistently blue. We do not follow up events with these characteristics that also lack an obvious host-galaxy counterpart.

[32] We have confirmed that this filter passes all candidates we found and classified in 2018.

[33] In this instance, and hereafter, when we refer to sources with peak brightness <18.5 mag, we mean a peak brightness in either the g or r filter of <18.5 mag.

[34] A subset of the >90 day events were also vetted, and no SNe were found.

remove any remaining CVs, AGNs, classical novae, and artifacts.

This singled out 17 likely SNe that our BTS filter scanning efforts had not picked up. Among these, nine were saved by other ZTF science programs or AMPEL, and were spectroscopically classified. The remaining eight are unclassified. The BTS sample contains 520 SNe peaking at $<18.5 \pm 0.05$ mag. This implies a completeness in our scanning of the BTS filter in 2018 of 97% for candidates with peak mag $\lesssim 18.5$. The 17 objects identified here are not included in our sample or analysis but will be included and analyzed in our next data release. We also note that Nordin et al. (2019) showed that ZTF has been complete with respect to detecting SNe reported to TNS by other groups when they fall on active ZTF CCD regions.

2.3. Spectroscopic Follow-up Assignment

The primary classification instrument of BTS candidates is the SEDM (Blagorodnova et al. 2018; Rigault et al. 2019). For candidates that pass the BTS filter (Section 2.1) and visual inspection (Section 2.2), we assign spectroscopic SEDM observations with the following priorities: transients that are, or are likely to become, brighter than 18.5 mag are scheduled with the highest priority (P3). Transients that appear likely to peak between 18.5 and 18.75 mag are assigned a lower priority (P2), and transients expected to peak fainter than 18.75 mag are triggered at the lowest priority (P1). For a typical BTS source ($m \approx 18.5$ mag) observed under typical observing conditions for 1800 s, SEDM obtains a signal-to-noise ratio $(S/N) \approx 12$ per resolution element and an integrated $S/N \approx 50$ in the region covered by the r_{ZTF} filter.

The SEDM queue is designed so that lower priority targets (e.g., P1, P2) are only observed if no higher priority targets are present in the queue that could be observed within the same observation-time window. The purpose of this priority scheme is twofold. First, it ensures that we can reach a high level of completeness for $m_{peak} < 18.5$ mag sources by allowing some margin for error on the fainter end of 18.5 mag. Second, when the queue allows (e.g., periods of consistently good weather), significantly fainter targets, including those as faint as ~ 19 mag, can also be observed in addition to our high-priority (P3) targets.

By default, triggers that enter the SEDM queue remain active for 7 days. If the transient has not been observed at this time, the candidate is reassigned to SEDM or to larger telescopes if the candidate has become too faint for SEDM ($m \gtrsim 19$ mag). Larger telescopes are also used if classification with SEDM is unsuccessful, which typically happens only if the candidate was observed in poor sky conditions, there is strong host-galaxy contamination, or if higher resolution is needed for a secure classification. For this purpose, we have primarily used P200 and Keck I, but supporting observing programs at LT, NOT, and APO have contributed significantly as well. Community efforts (e.g., ePESSTO; Smartt et al. 2015) have also contributed through TNS (see Section 3.1 for details).

2.3.1. Spectroscopic Completeness

A key goal for the BTS is to obtain high spectroscopic completeness for all events passing our basic selection criteria (essentially, $m < 18.5$ mag and extragalactic; see Section 2.1). While we made every effort to spectroscopically classify every

transient saved to the BTS program, our efforts were inevitably imperfect. Following the conclusion of 2018 (i.e., the period covered in this early release paper), we conducted two independent tests of our completeness as described below.

As an initial test of the completeness of BTS spectroscopic follow-up, we compiled every object that was saved following visual inspection (Section 2.2) and applied additional filters designed to remove most variables and AGNs using a more sophisticated point-source coincidence check and the long-term lightcurve history.[35] We restrict these candidates to those brighter than $m < 18.5$ mag in at least one observation. Every such object without a formal spectroscopic classification (74 in total) was then visually examined by our team of scanners. Most of these events are clearly not transients (e.g., subtraction artifacts, AGNs, stars) based on their full lightcurves. However, 31 events had properties consistent with SNe and were unclassified. If each of these events is a genuine SN, this would suggest a completeness of $\sim 96\%$.

We separately examined the filtered subset of alerts described above and estimated the characteristic rise and fade times (from and to 0.75 mag below peak, respectively) for every event using an automated procedure. For events with sufficient P48 data around peak to accurately constrain the rise and fade times, and with rise times between 4 and 100 days and fade times between 10 and 200 days (i.e., probable SNe), our classification completeness rate is 100% to $m_{peak} < 16.5$ mag, 98.8% to $m_{peak} < 17.5$ mag, 93.6% to $m_{peak} < 18.5$ mag, and 88.8% to $m_{peak} < 19.0$ mag. This method, which is easily automated (and could be applied to samples larger than what can be manually inspected), is consistent with the results from our visual inspection described above.

3. BTS SN Classifications

3.1. Classification Method

As previously noted, spectroscopic observations of BTS SN candidates are primarily obtained with SEDM. In cases where the candidates were too faint to be observed with SEDM, or scheduling conflicts prevented SEDM observations, or the SEDM spectra proved to be ambiguous, spectra were obtained with spectrographs on larger aperture telescopes: the Double Spectrograph (DBSP; Oke & Gunn 1982) on P200, the Low Resolution Imaging Spectrometer (LRIS; Oke et al. 1995) on the Keck I telescope, the Dual Imaging Spectrograph (DIS) on the APO 3.5 m telescope, the Spectrograph for the Rapid Acquisition of Transients (SPRAT; Piascik et al. 2014) on the 2.0 m LT, and the Alhambra Faint Object Spectrograph and Camera (ALFOSC) on the 2.56 m NOT.

SEDM data were reduced by the pipeline described in Blagorodnova et al. (2018) for data until 2018 August and by the automatic PYSEDM pipeline described in Rigault et al. (2019) for data after 2018 August. DIS data were reduced with the pyDIS package (Davenport et al. 2016). DBSP data were reduced using the PyRAF-based (Science Software Branch at STScI 2012) pipeline pyraf-dbsp (Bellm & Sesar 2016). ALFOSC data were reduced using standard procedures and tools based on IRAF (Tody 1986). LRIS data were reduced using the LRIS automated reduction pipeline (LPipe; Perley 2019).

---

[35] All but three of the early release SNe passed these additional filters. These three were rejected due to their proximity to bright stars, meaning the additional filters still find genuine SNe with high fidelity.

For SN candidates where we could not obtain spectroscopic observations from any of the above-mentioned telescopes, public TNS spectra were analyzed from the following instruments: the Asiago Faint Object Spectrograph and Camera (AFOSC) on the Asiago Ekar 182 cm telescope, FLOYDS on the Faulkes Telescope South (FTS) in Australia operated by Las Cumbres Observatory (LCO), the Wide Field Reimaging CCD (WFCCD) on LCO's duPont telescope, the ESO Faint Object Spectrograph and Camera v.2 (EFOSC2) on the New Technology Telescope (NTT), the Dolores (Device Optimized for the LOw RESolution) on the Telescopio Nazionale Galileo (TNG), the Intermediate-dispersion Spectrograph and Imaging System (ISIS) on the William Herschel Telescope (WHT), and the DeVeny spectrograph on the Discovery Channel Telescope (DCT).

Preliminary classifications are made via `SuperNova IDentification` (`SNID`; Blondin & Tonry 2007) template matching and visual inspection. `SNID` is automatically applied to all SEDM spectra, whereas for all other instruments, `SNID` is applied to the spectra by the observer. These preliminary classifications are annotated and recorded within the BTS program on the GROWTH `Marshal` and subsequently sent to TNS within 1 to 2 days.[36]

We revisit each of the preliminary classifications for this study in order to develop a homogeneous classification scheme. For this purpose, we developed a custom process to spectroscopically classify the 761 SNe in the BTS sample. For each BTS SN, we identified the top 15 spectral matches ($r\mathrm{lap}_{min} \geqslant 5$) from `SNID` to the most recent spectrum available on the GROWTH `Marshal`. We used the latest spectrum from the Marshal under the assumption that BTS targets only received additional spectroscopic observations when the initial classification was inconclusive. The `SNID` templates used for this process include the developer defaults,[37] as well as SNe Ia and a few non-SN templates from the Berkeley SN Ia program (BSNIP; Silverman et al. 2012); SN Ib/c templates from Modjaz et al. (2014), Liu et al. (2016), Modjaz et al. (2016), and Williamson et al. (2019); and SN IIP templates from Gutiérrez et al. (2017).

Following the SNID matching, we produced plots showing a comparison between the observed BTS spectrum and the (redshift-corrected) template spectrum from SNID. These plots were visually inspected to identify the best-matching template. In practice, the sample was split into six groups, and each group was inspected by a member of our team (C.F., A.A.M., A.D., Y.S., K.T., A.G.). While identifying the best-matching template, we recorded the SN type and redshift, as well as the name and phase of the template SN spectrum. In cases where the same classification was reported for all 15 matches, we recorded the type, redshift, and phase from the top match from the SNID output. We otherwise selected the best match based on common prominent SN spectral features (H, He, Si, Ca, Fe, etc.). If the top 15 matches from SNID proved ambiguous, we used either the ZTF lightcurve or alternative spectra to remove the ambiguity. For example, in cases with multiple matches to both SNe Ia and SNe Ic, the telltale secondary near-infrared (nIR) peak of SNe Ia can

typically be seen in ZTF r_{ZTF}-band lightcurves. The secondary nIR peak is unique to SNe Ia, as explained in Kasen (2006). It occurs following a recombination transition of the iron-group elements in the ejecta, whereby the strength of the Fe III and Co III lines decreases, and there is a corresponding strengthening of the Fe II and Co II lines (see also Blondin et al. 2015). While these papers have mostly considered $\lambda \gtrsim 7500\,\text{Å}$, a related "shoulder" in the r-band lightcurve is also observed at approximately the same time (Papadogiannakis et al. 2019a, 2019b).

If at this stage a classification still proved ambiguous, then the SN was examined by another member of the team. For consistency, a final check of all ambiguous classifications was performed by two members of the team (C.F., A.A.M.). Ultimately, we have classified 761 SNe via their spectra and lightcurves (Table 1). Out of these, 503 were classified using SEDM spectra, 86 using P200-DBSP, 76 using Keck I-LRIS, 20 using LT-SPRAT, 11 using APO-DIS, and 9 using NOT-ALFOSC. Finally, 56 were classified based on publicly available spectra on TNS.

We note that the positions reported in Table 1 are obtained by taking the weighted average of the position of the SN in every image in which the SN is detected (i.e., for every alert associated with the SN). The updated positions are more accurate than those reported to TNS, which typically only include a single low-S/N detection of the SN.

3.2. Classifications

We broadly classify all BTS SNe as belonging to one of four different classes: SNe Ia, SNe II, SNe Ib/c, and superluminous SNe (SLSNe). As detailed above, these classifications are primarily made via the SN spectra; however, in some cases the photometric evolution of the SN also informs the classification. This is especially true of the SLSNe, which are defined by their luminosity (typically $M < -21$ mag, Gal-Yam 2012; although ZTF adopts $M < -20$ mag).

Of the 761 SNe, we find that 547 are SNe Ia, 155 are SNe II, 40 are SNe Ib/c, and 19 are SLSNe. The fraction of discoveries belonging to each of these classes is in agreement with the results from Li et al. (2011) for a magnitude-limited survey, as shown in Figure 3.[38] Figure 3 also shows the relative rate of SNe found by ASAS-SN (Holoien et al. 2017a, 2017b, 2017c, 2019), which, like the ZTF BTS and unlike LOSS, does not target specific galaxies when searching for transients.[39] Both ZTF and ASAS-SN find a higher fraction of SNe II than LOSS, although these estimates all agree to within the uncertainties. By targeting massive galaxies, including a significant fraction of passive elliptical galaxies, LOSS may have been slightly biased against finding CC SNe (see Taubenberger 2017 and references therein). The relative rate of SLSNe is somewhat higher for ZTF compared to ASAS-SN, but still consistent within the uncertainties (see Section 3.3.4).

---

[36] The BTS classifications on TNS should also be considered preliminary. They reflect the initial classifications on the GROWTH `Marshal`, as turnaround speed is important, but they are subsumed by the efforts described in this paper.
[37] https://people.lam.fr/blondin.stephane/software/snid/#Download

[38] The ZTF BTS utilizes a 3 day cadence (see Section 2), whereas Table 7 in Li et al. (2011) reports results for surveys with a 1 day and 5 day cadence. The results in Li et al. (2011) are identical for 1 day and 5 day cadences, and thus we assume an intermediate 3 day cadence would also yield identical relative fractions of SNe.
[39] To calculate the relative rates of SNe found by ASAS-SN (and host-galaxy offsets, which are discussed below), we include both ASAS-SN discoveries and SNe recovered by ASAS-SN, as all discovered and recovered SNe are included in our analysis of the ZTF BTS. Therefore, the numbers shown here differ slightly from what is shown in, e.g., Figure 1 of Holoien et al. (2019), which only considers SNe discovered by ASAS-SN.
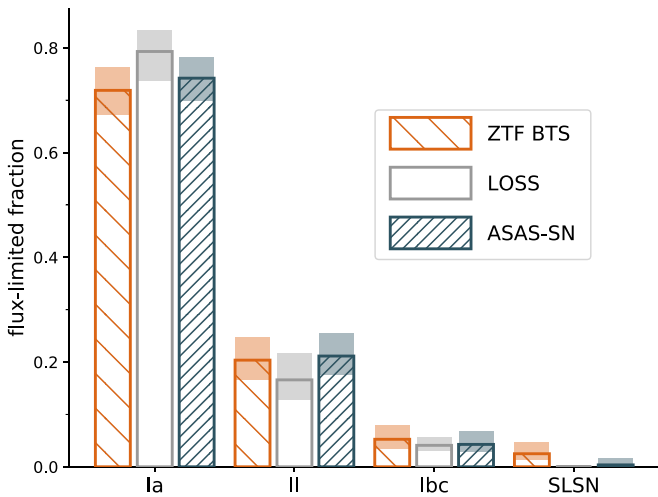
Figure 3. Relative fractions of SNe Ia, II, Ib/c, and SLSNe in the flux-limited ZTF BTS survey. The orange hatched bars show the results for the BTS, while the light-gray open bars show results from LOSS (Li et al. 2011), and the blue double-hatched bars show the results from ASAS-SN (Holoien et al. 2019). The lightly shaded regions show the uncertainty on each estimate (see text for further details). To within the uncertainties, the results agree for all three surveys (Li et al. 2011 did not report results for the SLSN class—see text).

Table 2 summarizes the relative fraction of SNe in each class for the ZTF BTS, ASAS-SN, and LOSS. For LOSS, we directly use the estimates from Li et al. (2011), while for the BTS and ASAS-SN, we assume the observations are drawn from a multinomial distribution and estimate 95% confidence intervals on the true rate via the approximate method of Goodman (1965) as implemented in the `MultinomCI` (Signorell et al. 2019) package in `R`. The true uncertainties on these fractions require a detailed estimate of the completeness of the BTS, which is beyond the scope of this paper, and will be addressed in future work (J. Nordin et al. 2020, in preparation).

As a test of our classification accuracy, we compare our final classifications to those made by ePESSTO (Smartt et al. 2015).[40] There are 26 sources in common between our BTS classifications and those made by ePESSTO, and the classifications are in agreement for all but two sources: ZTF18abmrhom (SN 2018ffi) and ZTF18abtswjk (SN 2018gfx). We classify ZTF18abmrhom as an SN Ia, whereas the ePESSTO spectrum is classified as having just galaxy light. The ZTF spectrum of ZTF18abmrhom, which was obtained two nights prior to the ePESSTO spectrum, shows clear and strong Si II absorption. The same broad feature can be seen in the ePESSTO spectrum, which is otherwise dominated by emission from the host galaxy. Furthermore, the r_{ZTF}-band lightcurve shows a "shoulder" a few weeks after maximum light. Taken together, it is very likely that ZTF18abmrhom is an SN Ia. The classification of ZTF18abtswjk is more challenging: the spectrum clearly shows narrow emission lines, and we have classified the event as an SN IIn, whereas ePESSTO classified the spectrum as an AGN. The photometric evolution of ZTF18abtswjk is far more reminiscent of SNe than AGNs: the transient exhibits a ~30 day rise, followed by a very slow, monotonic decline (the transient has exhibited a monotonic

fade by ~1.5 mag over the period covering 2018 and 2019) as is characteristic of many SNe IIn (e.g., Turatto et al. 1993). Furthermore, the WISE colors for the host galaxy are not consistent with AGNs (Jarrett et al. 2011). Thus, based on our comparison to ePESSTO, we conclude that our classifications are of high fidelity.

There were three BTS sources for which we attempted spectroscopic classification, but the nature of the transients remains unresolved. Each of the three candidates are positionally coincident with the nucleus of their host galaxies. ZTF18aaqkdwf (SN 2018fhd) exhibits a broad rise and decline over ~200 days and significant P-Cygni-like feature around Hα. However, variability at the location of ZTF18aaqkdwf was detected ~3.5 yr prior to the 2018 variability by iPTF, and the host galaxy is a bright point source in the radio (Helfand et al. 2015). Thus, the variability may be due to an AGN. The lightcurve of ZTF18abuqhje (SN 2018gki) has poor coverage with only four r_{ZTF} detections that show a decline of ~0.7 mag over ~15 days. We obtained two spectra of ZTF18abuqhje, both of which show many narrow lines that could be consistent either with an AGN or an SN IIn. However, we detected variability from this nucleus ~2.5 yr prior to 2018 with iPTF, which would be consistent with an AGN. The general evolution of the ZTF18aarcchg (AT 2018boa) r_{ZTF} lightcurve is consistent with an SN: the transient rises by ~1.5 mag over ~20 days, followed by a monotonic decline. Spectra of ZTF18aarcchg exhibit a blue continuum with a superposed narrow emission from the Balmer series, [O III], and [S II], all of which are consistent with star formation (the host is classified as a star-forming galaxy; Maraston et al. 2013). Without discernible SNe features in the spectrum, we cannot classify this transient. We exclude these three candidates from the subsequent analysis.

3.3. Subtype Classifications

The primary purpose of this study is to improve the measurement of the RCF and to extend the redshift coverage of this measurement beyond what is presented in Kulkarni et al. (2018). To that end, we only need to separate SNe Ia from all other transients in the ZTF BTS. Nevertheless, we attempt to make subtype classifications, based on the `SNID` matches described above, as detailed for each class below. We caution, however, that the vast majority of these classifications are made with very low-resolution ($R \approx 100$) SEDM spectra, and as a result, there are significant uncertainties on the subclass of any individual SN. Furthermore, any biases in the `SNID` template set can influence the final BTS classifications. The `SNID` templates were compiled from heterogeneous sources and do not perfectly reflect the discovery space of an untargeted transient survey, meaning the `SNID` templates themselves are a further source of uncertainty for the final subclassifications presented in Table 1 (see Blondin & Tonry 2007 for further details).

3.3.1. SNe Ia

The vast majority of SNe Ia discovered in magnitude-limited surveys are considered "normal." It is argued in Li et al. (2011) that the most common subclass of SNe Ia is SN 1991T-like (SN Ia-91T in Table 1), which are slightly overluminous relative to normal SNe Ia, followed by SN 1991bg-like (SN Ia-91bg in Table 1), which are underluminous and decline faster than

---

[40] We adopt ePESSTO for comparison because (i) it is the survey with the most overlap with the ZTF BTS, and (ii) all ePESSTO classifications are made with the 3.6 m NTT, which, on average, will perform better than SEDM for SN classification.

Table 2
Relative SN Rates

Survey	$\mathcal{R}(Ia)$	N_{Ia}	$\mathcal{R}(II)$	N_{II}	$\mathcal{R}(Ibc)$	N_{Ibc}	$\mathcal{R}(SLSN)$	N_{SLSN}
LOSS	$0.792\pm^{0.044}_{0.055}$	...	$0.166\pm^{0.050}_{0.039}$	...	$0.041\pm^{0.016}_{0.013}$	...	...	...
ASAS-SN	$0.742\pm^{0.040}_{0.045}$	607	$0.211\pm^{0.043}_{0.037}$	173	$0.043\pm^{0.024}_{0.016}$	35	$0.004\pm^{0.012}_{0.003}$	3
ZTF BTS	$0.719\pm^{0.043}_{0.048}$	547	$0.204\pm^{0.043}_{0.038}$	155	$0.053\pm^{0.027}_{0.018}$	40	$0.025\pm^{0.021}_{0.012}$	19

Note. Relative rates $\mathcal{R}$ of SNe Ia, II, Ibc, and SLSN from a flux-limited search. Results for LOSS are taken directly from Table 7 in Li et al. (2011) for a 1 day cadence and are based on an assumed luminosity function and Monte Carlo simulations. Thus, the total number of each type of SN is not relevant and therefore not reported. Results for ASAS-SN use all discovered and recovered SNe reported in Holoien et al. (2017a, 2017b, 2017c, 2019). Uncertainties for both ASAS-SN and the ZTF BTS include 95% confidence intervals (see text).

normal SNe Ia. This conclusion is derived from LOSS, which targeted relatively massive, high star formation rate galaxies. SNe Ia-91T seem to prefer late-type galaxies and may be associated with young stellar populations (e.g., Howell 2001). Thus, the relative rate of SNe Ia-91T may have been overestimated (see, e.g., Silverman et al. 2012; Taubenberger 2017).

In the ZTF BTS, we identify 504 normal SNe Ia, 31 91T-like SNe, and 6 91bg-like SNe. This represents significantly less 91T-like (∼6%) and 91bg-like (∼1%) SNe than one would expect based on the LOSS results for a magnitude-limited survey (∼18% 91T-like and ∼3% 91bg-like SNe; Li et al. 2011); however, it does agree with what is found by ASAS-SN (∼6% 91T-like and ∼1% 91bg-like SNe; Holoien et al. 2017a, 2017b, 2017c, 2019).

We caution that subtype classification can be difficult with a single low-resolution SEDM spectrum, as is the case for the majority of the SNe in our sample. For example, the most distinguishing feature of 91T-like SNe is weak Si II and Ca II absorption prior to maximum light (e.g., Filippenko 1997; Branch et al. 2006). At $R \approx 100$, even relatively strong absorption features can be smeared out, and as a result, SNID frequently identifies both normal and 91T-like SNe Ia as the best matches for the SNe Ia in our sample. Furthermore, it is difficult to separate normal and 91T-like SNe in post-maximum spectra. Thus, we conservatively label SNe Ia as normal, unless there is strong spectroscopic (very weak Si II and Ca II) or photometric (overluminous and a slow decline) evidence to support a 91T-like classification. Similarly for 91bg-like SNe, unless there is strong spectroscopic (weak Fe II, strong Ti II; Filippenko 1997) and photometric (underluminous and a fast decline) evidence, we label the SN as normal.

In addition to the above subclasses, we additionally identify the following: three SN 2002cx-like SNe based on their low luminosities and low ejecta velocities (SN Ia-02cx in Table 1), one SN Ia that shows signs of CSM interaction based on its high luminosity and intermediate-width Hα emission (SN Ia-CSM in Table 1), and two SNe that appear to be super-Chandrasekhar mass explosions based on their high luminosities and low velocities (SN Ia-SC in Table 1). A subset of these peculiar SNe Ia is classified and discussed in more detail in Yao et al. (2019).

3.3.2. SNe II

We have identified 162 H-rich SNe in the ZTF BTS. Of these, we make no effort to distinguish between Type IIP and IIL SNe, which are photometrically defined subtypes. We classify SNe II as either "normal" (119 of the 162), IIb (15), IIn (19), SLSNe-II (7; see also Section 3.3.4), or SN 1987A-like (2; SN II-87A in Table 1).[41] The relative fraction of SNe IIb and SNe IIn is significantly smaller in the BTS than that reported from LOSS (Li et al. 2011). This could be a direct consequence of the different targeting strategies, although there is one important caveat for SNe IIn: for SEDM spectra, SNe IIn represent the most difficult subclass to positively identify because the narrow emission that is the hallmark of SNe IIn (see Schlegel 1990) can easily be confused with emission lines from the host galaxy. When SEDM spectra indicate the presence of strong narrow H emission, we have generally attempted to obtain higher resolution spectra. However, some SNe IIn may not have strong-enough narrow lines to be noticed in an SEDM spectrum. These would be classified as SNe II. In conclusion, SNe identified as Type IIn in the BTS all have clear evidence for strong Hα emission lines that are significantly broader than would be expected from a galaxy or H II region.

SNe for which there were both Type II and IIb SNID matches have been visually inspected and classified by comparing the absolute and relative strengths of the H and He features (both emission and absorption) to those seen in typical hydrogen-rich SN II spectra. The two SN II-87A events exhibit a nearly identical spectroscopic evolution to SN 1987A itself, as well as the highly unusual lightcurve with an initial decline followed by a ∼100 day long rise (see, e.g., Arnett et al. 1989; McCray 1993).

3.3.3. SNe Ibc

There are 40 H-poor core-collapse SNe in the BTS (excluding 12 SLSNe-I; see Section 3.3.4). We classify these sources as either SNe Ib (11), Ic (18), Ic-BL (5), Ib/c (3), Ibn (2), or Ic-pec (1). The relative ratio of SNe Ib to Ic in the BTS sample is in agreement with that found by LOSS (Li et al. 2011), though we note that for both surveys the total number of stripped-envelope SNe discovered is relatively small and thus the uncertainties on the relative rates are high.

The SNe Ib clearly show He in their spectra, whereas the SNe Ic do not. There are three events that clearly lack H emission, but where we cannot distinguish between either a Ib or Ic classification (designated as SN Ib/c). The five SNe Ic-BL show very broad absorption features, similar to SN 1998bw (Patat et al. 2001), while the two SNe Ibn display the hallmark narrow He emission lines that define the subtype (Foley et al. 2007; Pastorello et al. 2007). Finally, there is a single event, ZTF18aceqrrs (SN 2018ijp), that lacks both H and He, but has a highly unusual spectroscopic and photometric evolution (L. Tartaglia et al. 2020, in preparation). Thus, we refer to ZTF18aceqrrs as a "peculiar" SN Ic (Ic-pec in Table 1).

---

[41] In Table 2, SLSNe-II are treated as part of the SLSN class and not the SN II class.

3.3.4. SLSNe

A population of so-called "superluminous" SNe, with peak optical luminosities (M_V up to -23 mag) greatly in excess of any known SN at the time, was first identified in the late 2000s (Quimby et al. 2007) and quickly recognized to occur in both hydrogen-rich (SLSN-II) and hydrogen-free (SLSN-I) varieties (Smith et al. 2007; Gal-Yam et al. 2009; Quimby et al. 2011). More recent surveys have shown that the luminosity distributions of both types of SLSNe overlap with "ordinary" Type IIn and Ic SNe (De Cia et al. 2018; Angus et al. 2019), and the spectral properties may also form a continuum. Thus, the identification of a particular luminous transient as a super-luminous SN, versus merely a luminous SN Ic or IIn, is a challenge. Work by Quimby et al. (2018) does indicate that SLSNe-I can be classified with spectral features alone without any luminosity cut. Quimby et al. (2018) show several SLSN-I events with peak luminosity below the traditional -21 mag threshold. However, it is still true that post-peak spectra for SLSNe-I and SNe Ic can be very similar (Pastorello et al. 2010). For the purposes of this analysis, we use spectroscopic matches to previous "unambiguous" SLSNe-I as the primary determinant, but also place any transient with $M_g < -20$ mag in this category even if it is well fit by ordinary SNe (as is the case for nearly all SLSNe-II, which are good matches to SNe IIn).

In total, we identify 19 SLSNe in the BTS sample. Of these, 12 are classified as H poor (SLSN-I), and the remaining 7 have H emission lines (SLSN-II). This represents $2.5\%\pm_{1.2}^{2.1}$ of the sample—which is, not surprisingly, a far higher fraction than what was found in galaxy-targeted surveys such as LOSS. LOSS found a single SLSN (SN 2006gy; Foley et al. 2006), which was not recognized as part of a separate class in Li et al. (2011). SLSNe are volumetrically rare and best found via untargeted wide-area surveys (Quimby et al. 2011). The relative rate of SLSNe in ASAS-SN is $0.4\%\pm_{0.3}^{1.2}$. This is lower but still consistent with our BTS estimate within the uncertainties on both measurements.

The true fraction of SLSNe may be even higher than what we report here: over this early-survey period, our selection methods were biased against SLSNe, because these very long-lived and slow-rising transients were often present in the reference image, such that at peak, the subtraction of their own pre-maximum flux made them appear fainter than they really were and thus less likely to pass the BTS filter.

The detailed analysis of the four SLSNe-I discovered during the ZTF commission phase has been submitted for publication by Lunnan et al. (2019), and a thorough investigation of the full ZTF SLSN sample is underway.

4. SN Distances and Host Galaxies

As in Kulkarni et al. (2018), our aim is to measure the RCF of local galaxy catalogs, in this case using SNe from the ZTF BTS. In order to make this measurement, we need to both identify the host galaxy for every SN and measure the SN redshift (for cases where the host redshift is unknown). Using this information, it is then possible to calculate the RCF.

4.1. SN Redshifts

In addition to providing SN spectral types, SNID estimates the redshift of the SN it is attempting to classify. We adopt the redshift of the best-matching SNID template as the redshift of

the SN, z_{SN}.[42] The redshift distribution for BTS SNe is shown in Figure 4, where we adopt the redshift of the host galaxy (z_{host}) when known; otherwise, we show z_{SN}.

We can estimate the accuracy of the SNID redshift measurements using the subset of BTS SNe that have host galaxies with known redshift (for more on the identification of BTS host galaxies, see Section 4.2). We find that z_{SN} is a good estimator of the host-galaxy redshift, z_{host}, as summarized in Figure 5 for the 345 ZTF BTS host galaxies with known redshifts.

The main panel in Figure 5 shows the difference between z_{SN} and z_{host} as a function of z_{host}. The residuals show that for SNe Ia, there is a relatively small scatter ($\sigma \approx 0.0037$)[43] and virtually no bias in the estimates of z_{SN}. The scatter is somewhat higher for CC SNe ($\sigma \approx 0.0047$), where SNID appears to systematically overestimate the true redshift, as is seen in the Gaussian kernel density estimate (KDE) shown in the right panel of Figure 5. We find some evidence for an increased scatter at higher redshifts. For SN Ia hosts with $z \leqslant 0.04$, $\sigma \approx 0.0032$, while for hosts with $0.08 \leqslant z < 0.12$ $\sigma \approx 0.0045$ (though the 90th percentile widths are nearly identical in these two regions). This increased scatter makes sense as the S/N typically decreases for higher redshift SNe; for SNe outside the redshift range shown in Figure 5, the typical uncertainty on any individual redshift may be larger than $\sim$0.004. We also find that the scatter is not appreciably larger when restricting the sample to only those SNe that have been observed by SEDM. In the analysis that follows, we assume that $z_{host} = z_{SN}$ for normal SNe Ia, and that the typical uncertainty on z_{SN} is 0.004. We note that (i) this is very consistent with the uncertainty ($\sigma = 0.005$) reported in Figure 19 in Blondin & Tonry (2007), even though a very different redshift range was used ($z = 0.1$–0.8), and (ii) our estimated redshift uncertainty on z_{SN} is much larger than the uncertainty in the wavelength calibration of SEDM (Figure 13 in Rigault et al. 2019). These two findings indicate that the accuracy of our SNID-based redshifts (z_{SN}) is not limited by the low resolution of SEDM.

4.2. Host-galaxy Identification

Correctly associating a newly discovered transient with its host galaxy is a challenging problem, especially when the redshift of the host candidate is unknown. Simply identifying the closest galaxy (in angular offset) is likely to produce a significant number of misidentifications, especially in the case of nearby SNe for which angular offsets relative to the host nuclei may be quite large.

We use a combination of automated procedures and visual inspection to identify hosts for ZTF BTS SNe. As an initial pass, we query the NASA Extragalactic Database (NED)[44] for all galaxies within $2'$ of the SN position. Within this list, the galaxy with the smallest angular separation from the SN and a cataloged redshift in NED is automatically assigned as the host. In cases where there are no cataloged galaxy redshifts within $2'$ of the SN, the galaxy with the smallest angular separation from the SN is assigned as the host. In cases where the z_{host} and

---

[42] No corrections for heliocentric, galactocentric, or host-galaxy rotation velocity are applied to z_{SN}.
[43] We use a robust estimate of scatter by taking half of the difference between the 84th and 16th percentiles. The sample standard deviation is $\sim$0.005. The sample standard deviation for the recession velocity is $\Delta v/v \approx 0.14$.
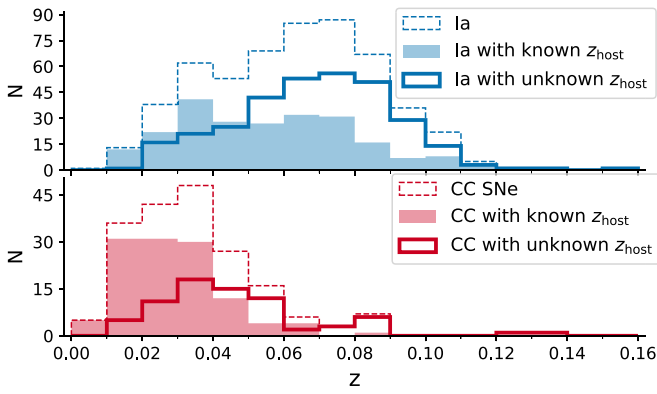[44] https://ned.ipac.caltech.edu/

Figure 4. Redshift distribution of BTS SNe Ia (top) and CC SNe (bottom) shown by thin dashed lines. SNe associated with host galaxies of known redshift are shown as solid histograms. If the host-galaxy redshift is unknown, we adopt z_{SN} as the host-galaxy redshift, as shown by the thick solid lines. SLSNe are not shown.
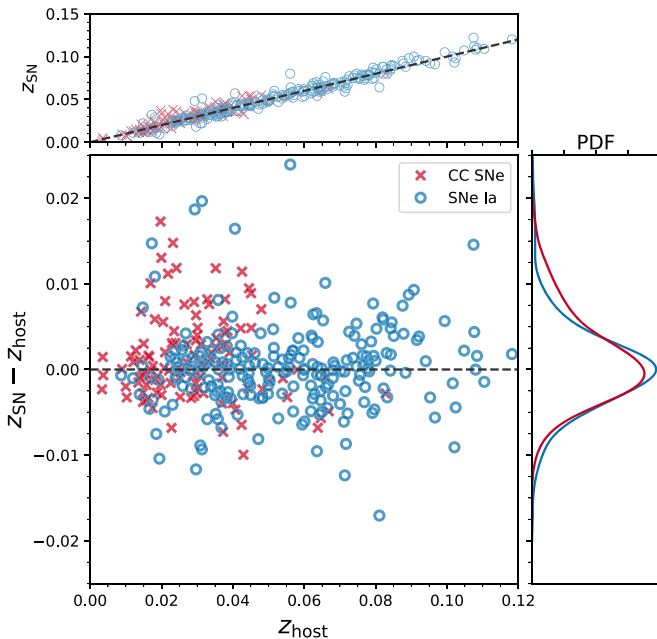

Figure 5. Difference between host-galaxy redshifts (z_{host}) and SNID-derived redshifts (z_{SN}) as a function of host-galaxy redshift. CC SNe are shown as crosses, while SNe Ia are shown as open circles. The scatter in the difference is nearly constant as a function of redshift. Top: z_{SN} vs. z_{host}. Right: a Gaussian KDE of the PDF of the residuals for CC SNe (red) and SNe Ia (blue). The typical scatter is ~0.004 (see text), while 95% of all SNe Ia have z_{SN} within 0.01 of z_{host}.

z_{SN} significantly differ ($|z_{SN} - z_{host}| > 0.05$), the galaxy with the smallest angular separation from the SN is assigned as the host. From here we calculated the projected separation, d_p, between the SN and the host galaxy using the redshift of the SN (see above). We visually inspect host candidates with a projected separation $d_p \geqslant 19$ kpc. In most of these cases, it is clear that the automated procedure identified a background galaxy that is clearly not the host, in which case we update the host with the NED galaxy with the smallest angular separation from the SN. Following this procedure, there were a total of 12 SN host identifications with separations $d_p \geqslant 19$ kpc (9 SNe Ia and 3 SNe II). In 11 of these 12, the host redshift is known and that redshift matches that of the SN, providing confidence in these associations. We cannot rule out the possibility that these

SNe occurred in faint dwarf galaxies that are associated with the bright galaxy that has been identified as the host. For the purposes of the RCF calculation below, we assume each of these identifications to be correct. For the remaining SN, ZTF18acrcetn (SN 2018jag), there is a very bright ($r' = 14.3$ mag) elliptical galaxy, PSO J015.9596+10.5902, in the field of the SN. The SN is ~3.2 Petrosian radii from the galaxy, which has an SDSS photometric redshift, 0.052 ± 0.012 (Abolfathi et al. 2018), that agrees with the SN redshift determined by SNID, 0.053 (which gives $d_p \approx 24$ kpc). For the calculations below, we assume that this identification is correct.

Following this procedure, we use deep i-band stack images from PS1 to visualize the position of each SN relative to its host galaxy. In the vast majority of cases, these images confirmed a clear association between the SN and host galaxy. In some cases, the putative host was extremely faint and a significantly brighter galaxy with only slightly larger angular separation was selected as the likely host. Finally, there were a handful of cases where the association was ambiguous or with a low-S/N PS1 detection. We find that for 40 SNe in the sample, the host identification is ambiguous. We exclude these SNe from the host-galaxy analysis below. We thus identify host galaxies for 721 of the 761 SNe in the ZTF BTS sample. Properties of the BTS SNe host galaxies are summarized in Table 3, including notes on each of the SNe identified as having ambiguous hosts. For the 40 ambiguous cases, we find that 29 SNe have no discernible host, including 17 SLSNe, for which host galaxies are typically not found in imaging at the depth of PS1 in this redshift range (e.g., Quimby et al. 2011). The remaining 11 are either roughly equidistant between multiple galaxies of the same brightness, or very close to a faint galaxy, with a significantly brighter galaxy at a similar redshift of the SN residing at much larger angular separation.

The host-galaxy coordinates available via NED come from a heterogeneous set of catalogs and surveys, resulting in an astrometric offset between NED galaxy coordinates and ZTF SN positions, which are measured relative to Gaia (Gaia Collaboration et al. 2016). We crossmatch the host positions against the PS1 catalog, which is also calibrated against Gaia, in order to place the BTS SNe and host galaxies on the same relative astrometric system. A total of 715 of our initial host positions have counterparts within $2''$ in the PS1 DR1 `MeanObject` table, which is astrometrically calibrated against Gaia. Four of the hosts, those associated with ZTF18aapgrxo (SN 2018bym), ZTF18aayjyub (SN 2018cod), ZTF18acaeous (SN 2018hbu), and ZTF18acrknyn (SN 2018jef), are too faint to be included in the PS1 `MeanObject` table, and instead, we use PS1 positions from the `StackObjectThin` table. The last two hosts, associated with ZTF18acbzoyh (SN 2018hqu) and ZTF18acdwohd (SN 2018ids), are not detected in the PS1 catalog, and we instead use their positions from SDSS and the Galaxy Evolution Explorer (GALEX; Martin et al. 2005), respectively, in Table 3. Following this update of the positions, we recalculate the distribution of host-galaxy separations, which is shown in Figure 6. We find a nearly identical distribution in projected separation for CC SNe and SNe Ia (middle panel of Figure 6). We use a two-sample Kolmogorov–Smirnov (KS) test and a χ^2 test for independence to determine the statistical difference between the two distributions and find no significant difference between the projected offsets of CC SNe and SNe Ia.

Table 3
BTS Host Galaxies

ZTF Name	Host Name	α_{host} (J2000.0)	δ_{host} (J2000.0)	z_{host}	SN Offset (arcsec)	d_p (kpc)	m_g (mag)	m_r (mag)	m_i (mag)	m_z (mag)	m_y (mag)	m_{W1} (mag)	m_{W2} (mag)	$E(B-V)$[a] (mag)
ZTF18aabssth	PSO J165.1878+22.2877	11:00:45.07	+22:17:15.8	0.02291	4.44	2.06	16.89	16.49	16.38	16.38	16.61	15.79	16.38	0.015
ZTF18aabxlsv	PSO J157.4639+09.0106	10:29:51.32	+09:00:38.1	0.04797	9.53	8.96	16.17	15.48	15.27	15.02	15.02	14.82	15.30	0.025
ZTF18aaemivw	PSO J158.4280+39.4908	10:33:42.72	+39:29:26.8	0.06807	0.33	0.43	16.66	16.03	15.67	15.53	15.35	14.94	15.08	0.012
ZTF18aagpzjk	PSO J119.8484+16.4214	07:59:23.61	+16:25:16.9	0.01631	26.83	8.91	14.96	14.49	14.33	14.49	14.87	13.85	14.43	0.031
ZTF18aagrdcs	PSO J218.3331+41.2658	14:33:19.95	+41:15:56.9	0.01814	5.43	2.00	18.53	17.62	17.45	18.11	18.86	17.32	18.00	0.012
ZTF18aagrtxs	PSO J198.6087+50.9792	13:14:26.08	+50:58:45.0	0.02966	7.94	4.72	...	...	...	13.77	13.68	13.70	14.36	0.010
ZTF18aagstdc	...	...	...	...	...	...	...	...	...	...	...	...	...	...
ZTF18aagtcxj	PSO J248.0475+42.7139	16:32:11.40	+42:42:50.0	0.03240	2.40	1.55	16.72	15.70	15.31	15.00	14.82	14.28	14.75	0.011
ZTF18aahesrp	PSO J128.9390+28.2705	08:35:45.35	+28:16:13.7	...	1.36	1.35	19.43	18.99	18.82	18.69	18.68	19.14	19.86	0.036
ZTF18aahfeiy	PSO J154.3116+43.5219	10:17:14.78	+43:31:18.8	0.07126	10.09	13.71	17.13	16.69	16.38	16.43	16.50	16.19	16.61	0.010
ZTF18aahfgyz	PSO J175.2822+24.8218	11:41:07.72	+24:49:18.5	0.01201	8.88	2.18	...	...	...	...	11.84	11.98	12.67	0.023
ZTF18aahfqbc	PSO J182.6357+39.4059	12:10:32.58	+39:24:21.1	0.00332	73.35	5.03	12.09	11.52	...	...	...	9.98	9.51	0.024
ZTF18aahfxnn	PSO J176.5486+09.3548	11:46:11.67	+09:21:17.1	...	4.35	6.12	18.89	18.49	18.20	18.22	18.09	18.09	18.69	0.026
ZTF18aahfzea	PSO J181.3610+20.3031	12:05:26.64	+20:18:11.1	0.02373	14.29	6.84	...	19.03	19.86	...	...	...	...	0.033
ZTF18aahheaj	PSO J195.1118+18.6197	13:00:26.83	+18:37:11.1	0.05272	4.74	4.87	18.24	17.79	17.73	17.95	17.82	16.69	17.07	0.022
ZTF18aahhenr	PSO J207.3615+26.4619	13:49:26.75	+26:27:42.7	0.07636	5.64	8.16	17.04	16.21	15.80	15.68	15.66	15.29	15.80	0.010
ZTF18aahhqih	PSO J138.7320+46.9031	09:14:55.68	+46:54:11.2	0.01425	5.22	1.52	14.06	13.53	...	14.07	13.44	12.62	13.09	0.016
ZTF18aahhzqn	PSO J178.7588+32.0746	11:55:02.11	+32:04:28.7	0.03106	12.34	7.67	15.55	15.07	14.87	14.71	14.64	14.77	15.23	0.020
ZTF18aahjafd	PSO J198.2744+23.4593	13:13:05.86	+23:27:33.5	0.03588	0.21	0.15	18.15	17.54	17.17	16.99	16.89	17.34	18.02	0.010
ZTF18aahmhxu	PSO J176.7668+19.5508	11:47:04.03	+19:33:02.9	...	0.62	1.77	19.77	18.98	18.54	18.40	18.24	18.06	18.38	0.027

Notes. Optical *grizy* photometry is taken from PS1 Kron magnitude measurements, while mid-IR *W*1 and *W*2 photometry are from `Tractor` and WISE (see text). All magnitudes are reported in the AB system, and no correction for extinction has been applied. The host galaxies for ZTF18acbzoyh (SN 2018hqu) and ZTF18acdwohd (SN 2018ids) are not detected in the PS1 catalog (see text).

[a] $E(B-V)$ is determined using the Schlafly & Finkbeiner ([2011](#)) updates to the Schlegel et al. ([1998](#)) maps.

(This table is available in its entirety in machine-readable form.)
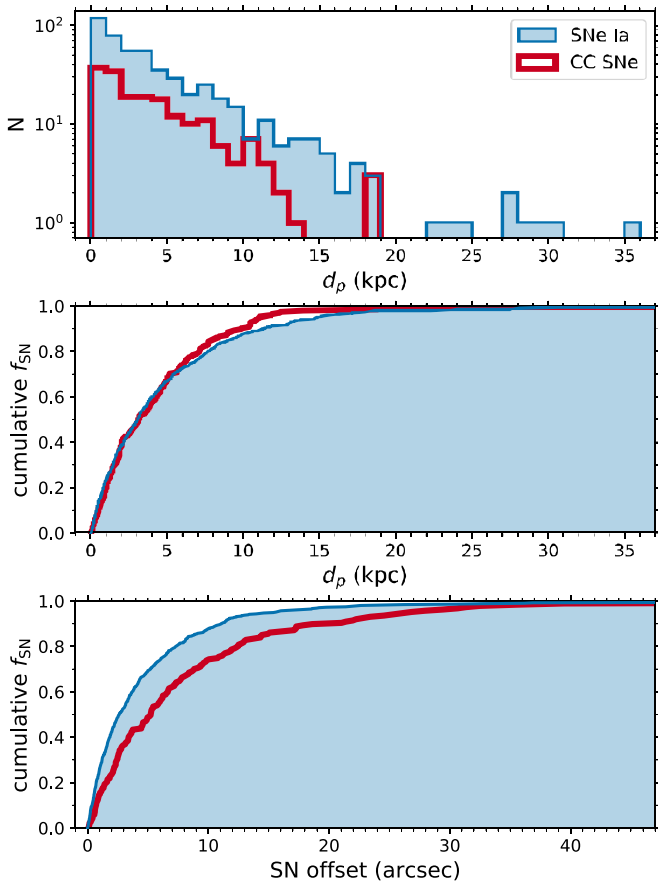
Figure 6. Top: projected physical separation d_p, in kiloparsecs, between ZTF BTS SNe and their respective host galaxies. SNe Ia are shown via a solid histogram, while CC SNe are shown via a thick crimson line. The general shape of these distributions are similar to what was found during PTF, with roughly an order of magnitude fewer SNe at $d_p \approx 10$ kpc as there are at $d_p < 1$ kpc (Kasliwal et al. 2012). Middle: cumulative distribution of d_p for BTS SNe and their hosts. The distribution for SNe Ia and CC SNe is nearly identical; the small discrepancies observed between $\sim$10 and 15 kpc are likely due to small number statistics. Bottom: cumulative distribution of the angular offset, in arcseconds, between BTS SNe and their hosts. Given that the average SN Ia is at higher redshift than the average CC SN in the BTS (Figure 4), but the physical separations are the same, it makes sense that SNe Ia, on average, have a smaller angular offset than CC SNe.

Using the newly identified host offsets, we can additionally examine whether or not there is a strong bias against finding nuclear SNe in ZTF, as has been found for other surveys (see Holoien et al. 2019). Figure 7 compares the cumulative distribution of angular offsets for bright ($m_{peak} \leqslant 17$ mag) BTS SNe and ASAS-SN.[45] We find remarkably similar distributions between ZTF and ASAS-SN. Both a two-sample KS test and a χ^2 test for independence do not show a statistically significant difference between the two samples. This suggests that ZTF is no more biased against finding nuclear SNe than ASAS-SN, in contrast to other surveys (e.g., Holoien et al. 2019). We caution that while the relative bias is comparable to ASAS-SN, both ASAS-SN and ZTF may have an unmeasured absolute bias against finding SNe in the nuclei of galaxies.

Following host identification, we need to determine the absolute magnitude of the host galaxies in order to measure the RCF (see Kulkarni et al. 2018 and below for further details). In this study,
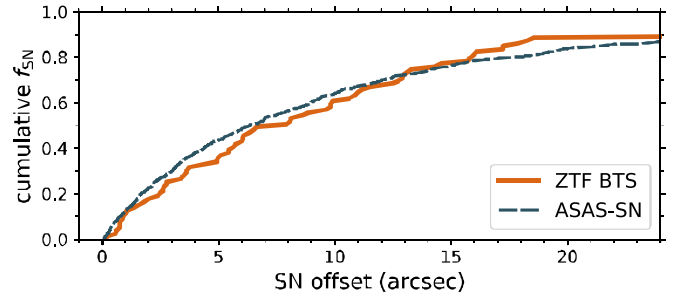
Figure 7. Cumulative distribution of the angular offset between $m_{peak} \leqslant 17$ mag SNe and their host galaxies found by the ZTF BTS (solid line) and ASAS-SN (dashed line). The distributions are generally very similar, with ASAS-SN doing slightly better at small separations ($<5''$); however, these differences may simply be due to small number statistics.

we focus on the mid-IR flux of the host galaxies, primarily for two reasons: (i) a galaxy's mid-IR absolute magnitude serves as a good proxy for the total galactic stellar mass (Wen et al. 2013), and (ii) mid-IR photons are mostly transparent to dust in the Milky Way, meaning that significant reddening corrections are not needed to estimate a galaxy's absolute magnitude in the mid-IR. The WISE (Wright et al. 2010) satellite conducted an all-sky survey in the mid-IR, and we use WISE images to determine the brightness of ZTF BTS SN host galaxies at 3.4 μm.

The largest WISE source catalogs (e.g., unWISE; Schlafly et al. 2019) utilize an unresolved (i.e., stellar) point spread function (PSF) to measure source flux. This PSF is not appropriate for many of the low-z galaxies in our sample, which are clearly resolved in WISE imaging. The recent development of The Tractor (Lang et al. 2016a) enables "forced" WISE flux measurements, where the mid-IR apertures are determined via sources detected in (relatively) high-resolution optical images. The Tractor was used to measure the mid-IR flux of $\sim$400 million WISE sources that were detected by SDSS (Lang et al. 2016b) and now is also being applied to Legacy Survey images (Dey et al. 2019). There are 371 BTS host galaxies that have Tractor forced mid-IR photometry from both Legacy Survey and SDSS images, while an additional 157 hosts have detections in just Legacy Survey images and another 90 hosts have detections in just SDSS[46] (hereafter we refer to this aperture-matched forced photometry as Tractor photometry). We include Tractor photometry based on both Legacy Survey and SDSS images in our analysis of the RCF below. For the 371 sources detected both in the Legacy Survey and SDSS, we compare the Tractor photometry derived from each set of images and measure a sample standard deviation of 0.008 in Δ flux/flux. This small difference suggests that there are no systematic effects introduced by combining photometry from the two different optical catalogs. Ultimately, this results in 618 host galaxies with 3.4 μm flux measurements that we can use in the analysis of the RCF. Including only the brightest mid-IR galaxies in our sample will bias our final measurement of the RCF, as discussed below.

5. The Redshift Completeness Fraction

To calculate the redshift completeness fraction (RCF), we follow the methodology originally outlined in Kulkarni et al. (2018). The RCF captures the probability that a random galaxy

will have a cataloged spectroscopic redshift as a function of its redshift and IR luminosity. To estimate the RCF, we use only SNe Ia, as they occur in both star-forming and passive galaxies, whereas CC SNe would only trace star-forming galaxies. When a ZTF BTS SN has a previously cataloged host-galaxy redshift, we consider that a "hit" (NED_z), and when the host does not have a known redshift, that is considered a "miss" (!NED_z).

By raw number, there are 512 SNe Ia with known hosts in the BTS,[47] and 227 of them are "hits" (have known redshifts). Thus, over the redshift range sampled by the BTS, the RCF = 44% ± 4% (90% confidence interval).[48] This estimate is significantly lower than what was found for a lower-redshift sample (Kulkarni et al. 2018 estimated RCF ≈ 75%). The difference in RCF estimates can be entirely understood by the differing redshift distributions of the two samples. If we restrict our analysis to SNe with $z \leqslant 0.03$, we find the RCF = 69% ± 4% (90% confidence interval), which is consistent with the results reported in Kulkarni et al. (2018). At face value, these results show that the RCF decreases as redshift increases, an unsurprising result.

We can further constrain the RCF as a function of redshift and galaxy luminosity by estimating the joint distribution for a galaxy to have a cataloged redshift given its redshift and M_{W1}, RCF(z, M_{W1}).[49] A detailed summary of the joint probability RCF calculation is included in the Appendix. To estimate RCF (z, M_{W1}), we include only those SNe Ia with identified host galaxies that have a measured IR brightness. This reduces the sample to 442 SNe, of which 213 are "hits." An estimate of this joint distribution, as well as the one-dimensional probabilities RCF(z) and RCF(M_{W1}), is shown in Figure 8. All 512 SNe Ia are used to constrain RCF(z), as a host-galaxy identification or brightness measurement is not necessary for that calculation.

From Figure 8, it is clear that the analysis in Kulkarni et al. (2018) was significantly limited by the lower-redshift sample that was available at that time. For example, there are no "hits" for $z > 0.12$, and the RCF(z) tends toward zero at high redshifts, whereas Kulkarni et al. (2018) only found mild evidence that the RCF(z) decreases with z. Unsurprisingly, we still find that low-z and massive galaxies are the most likely to be cataloged. At higher redshifts ($z > 0.1$), only very massive galaxies ($M_{W1} \lesssim -22$ mag AB, comparable to that of the Milky Way) are cataloged.

The decline in RCF(z) as a function of z has important ramifications for the electromagnetic (EM) follow-up of gravitational wave (GW) events. The typical localization areas for two- and three-detector networks is several hundred to several thousand square degrees (Kasliwal & Nissanke 2014). One strategy to mitigate against these large areas that would be impossible to search even with modest FoV instruments is to target known galaxies within the LIGO localization volume (e.g., Gehrels et al. 2016). During O3, the horizon distance for binary neutron star (BNS) mergers is ∼200 Mpc (see O3 alerts for S190425z, S190510g, S190901ap, and S190910h;
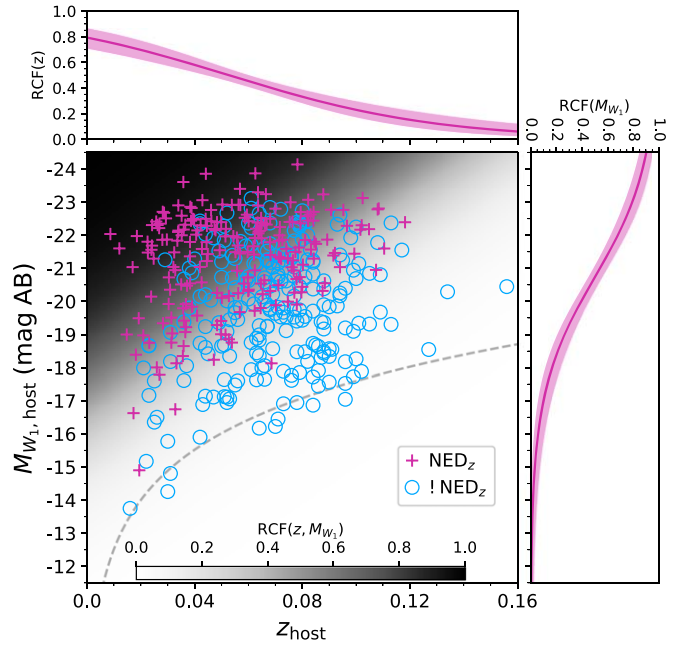
Figure 8. Absolute W_1-band magnitude, $M_{W1,host}$, vs. redshift, z, for the host galaxies of SNe Ia in the ZTF BTS. Galaxies with known redshifts (from NED or other databases) prior to SN discovery are shown as magenta pluses, while those lacking redshifts (!NED_z) are shown as blue circles. The dashed line roughly corresponds to the WISE detection limit $m_{W1,limit} \approx 20.629$ mag (Schlafly et al. 2019). The shaded background shows the probability of a host galaxy having a cataloged redshift given its redshift and M_{W1} (RCF(z, M_{W1})), based on 442 galaxies with WISE detections. The top and right plots show the probability of a host galaxy having a cataloged redshift given only its redshift, RCF(z), or M_{W1}, RCF(M_{W1}), respectively. In these two plots, the solid lines show the median value of the RCF, while the shaded region corresponds to the 90% credible region on the RCF.

(The data used to create this figure are available.)

Ligo Scientific Collaboration & VIRGO Collaboration 2019a, 2019b, 2019c, 2019d), roughly corresponding to $z \approx 0.05$. According to the BTS, for $z \leqslant 0.05$, the RCF ≈ 63%, while integrating our best model inference from $z = 0$–0.05 yields RCF ≈ 57%. Thus, targeted efforts to identify EM radiation from BNS mergers are likely to miss one-third, or more, of all potential host galaxies for the EM transient. These numbers become significantly worse for events discovered at a distance $z > 0.05$. Any future efforts to quantify the rate of EM counterparts to GW events should account for the fraction of "missing" galaxies that we have identified with the BTS.

5.1. Catalog Completeness as a Function of Galaxy Brightness

To date, SDSS has been the most prolific survey in terms of spectroscopically measuring galaxy redshifts, with ∼2.8 million cataloged galaxies and counting (Aguado et al. 2019). At this stage, significant improvements to the RCF will require tens of millions of new redshift measurements. Fortunately, within the next few years, we will enter the era of supremely multiplexed spectrographs (e.g., the 4 m Multi-Object Spectroscopic Telescope (4MOST),[50] the Dark Energy Spectroscopic Instrument (DESI),[51] the Subaru

---

[47] We exclude Ia-02cx, Ia-csm, and Ia-SC events from the RCF calculations. These "peculiar" events account for ∼1% of the BTS SN Ia sample and would not substantially change our analysis.

[48] As in Kulkarni et al. (2018), we find that the RCF traced by CC SNe is much higher than that traced by SNe Ia. This suggests that redshift catalogs are more complete for star-forming galaxies than passive galaxies.

[49] We convert observed $W1$ magnitudes to absolute magnitude by calculating the distance modulus with `astropy` (Astropy Collaboration et al. 2013), assuming a concordance cosmology with $\Omega_\Lambda = 0.7$, $\Omega_M = 0.3$, and $H_0 = 70$ km s^{-1} Mpc^{-1}. We also correct for Milky Way extinction, a small effect, using $E(B-V)$ from Schlafly & Finkbeiner (2011), $R_V = 3.1$, and the extinction law from Fitzpatrick & Massa (2007).

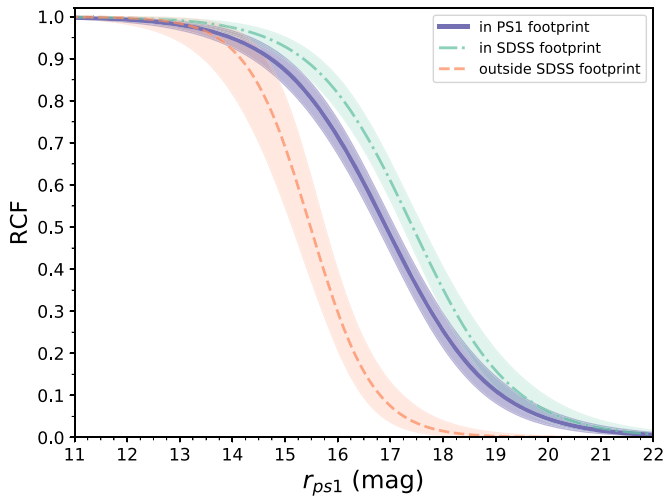[50] https://www.4most.eu/cms/
[51] https://www.desi.lbl.gov/

Figure 9. Redshift completeness fraction as a function of apparent host-galaxy brightness, as traced by the r_{PS1} Kron mag measurement. The solid purple curve shows the median value for all hosts in PS1 (95% of all identified ZTF BTS hosts), while the green, dotted–dashed curve shows hosts within the SDSS imaging footprint (72% of all hosts), and the orange, dashed curve shows hosts outside SDSS (23% of all hosts). The RCF is higher within the SDSS footprint, likely due to the many SDSS spectroscopic redshift surveys. For all galaxies within PS1, the RCF = 0.5 at $r_{PS1} \approx 16.9$ mag, while within the SDSS footprint, the RCF = 0.5 at $r_{PS1} \approx 17.4$ mag, and outside SDSS, the RCF = 0.5 at $r_{PS1} \approx 15.5$ mag.

(The data used to create this figure are available.)

Prime Focus Spectrograph (PFS),[52] Euclid,[53] the Wide Field Infrared Survey Telescope (WFIRST)[54]), which could dramatically increase the number of galaxies with known spectroscopic redshifts within the local universe. The best strategy to this end is to obtain spectra of bright galaxies with currently unknown redshifts, as is planned as part of the DESI Bright Galaxy Survey (DESI Collaboration et al. 2016). Using the same methodology described above, we can estimate the RCF as a function of galaxy brightness (as traced by the PS1 r band), rather than z or M_{W1}. The results from this exercise are summarized in Figure 9.

From Figure 9, it is clear that the vast majority of extremely bright galaxies ($r_{PS1} \lesssim 14$ mag) have cataloged redshifts. Figure 9 also shows the RCF for galaxies that are and are not within the SDSS imaging footprint,[55] and a comparison of these two curves highlights the crucial role that SDSS played in terms of identifying galaxies in the local universe and spectroscopically measuring their redshifts. SDSS pushes the completeness of redshift catalogs ~2 mag fainter than what is observed outside the SDSS footprint. From our analysis, it is possible to estimate the completeness of existing redshift catalogs as a function of depth, and we find that catalogs are currently ~90%, 50%, and 10% complete to a depth of $r_{PS1} \approx 14.7$ mag, 16.9 mag, and 19.1 mag, respectively. Because the DESI bright galaxy survey is an order-of-magnitude increase over SDSS, Figure 9 makes it clear that

the DESI bright galaxy survey will dramatically improve our knowledge of which galaxies reside in the local universe.

6. Summary and Conclusions

We have presented early results from the ZTF BTS. The BTS utilizes publicly announced discoveries from the ZTF MSIP surveys to spectroscopically classify all extragalactic transients that peak brighter than 18.5 mag. Simple filters are applied to the ZTF alert stream with the aim of minimizing false negatives, and we estimate that ~95% of all $m_{peak} \leqslant 18.5$ mag SNe in the BTS are spectroscopically classified (during the period of the survey in 2018). This effort has resulted in the classification of 761 SNe.

Spectroscopic observations are primarily conducted with SEDM, which is optimized to classify SNe with $m < 19$ mag. For sources that are inaccessible to SEDM, we utilize any available resource in order to obtain a classification. Final BTS classifications utilize spectral template matching, via SNID, and visual inspection of the spectra and (publicly available) lightcurves. Of the 761 classified BTS SNe, the majority are SNe Ia (547), followed by CC SNe, both SNe II (155) and SNe Ib/c (40), with a relatively small number of SLSNe (19). The relative fraction of each of these types of SNe agrees with what has been found in previous studies (Li et al. 2011; Holoien et al. 2019).

In this early release paper, we have focused on measuring the redshift completeness of local galaxy catalogs by using SNe Ia as a relatively unbiased tracer of galaxies in the local universe. By raw number, we find that less than half of the BTS SN host galaxies have known spectroscopic redshifts. In more detail, we find that the RCF falls steeply as a function of redshift, with only ~half of all galaxies having known redshifts at $z \approx 0.05$, and $\lesssim 20\%$ of galaxies having known redshifts at $z \approx 0.1$. The "missing" galaxies with unknown redshifts have important ramifications when searching for EM counterparts to multi-messenger astronomical events, and suggest that the most complete method to find the EM counterparts for events at $d \gtrsim 100$ Mpc is to tile the entire error regions associated with GW or neutrino event alerts. However, even if this is done, the same problem arises again when deciding which candidates among those found by the wide-field searches to follow up spectroscopically. Given the resources available, typically candidates with known distances, which also coincide with the distance constraints in a GW alert, are heavily prioritized for follow-up (e.g., Andreoni et al. 2019; Coughlin et al. 2019). Incorporation of redshifts from the Census of the Local Universe narrowband Hα catalog (Cook et al. 2019) may alleviate this problem to some extent in the near future.

The combination of ZTF and SEDM has illustrated the power of focused efforts in the era of very large time-domain surveys. Within the next few years, the Legacy Survey of Space and Time (LSST; Ivezić et al. 2008) will begin full survey operations. LSST will increase the volume of transient discoveries by an order of magnitude relative to ongoing surveys in much the same way that PTF, PS1, and others built upon LOSS, and ATLAS and ZTF have built upon those surveys. We have already reached the era where true spectroscopic completeness is impossible for SN surveys, and LSST will greatly exacerbate this problem. Nevertheless, the use of an ultra-low-resolution instrument has allowed us to spectroscopically classify a nearly complete subset of the discoveries made by ZTF (those with $m_{peak} \leqslant 18.5$ mag). The simple focus

---

[52] https://pfs.ipmu.jp/
[53] https://sci.esa.int/web/euclid/
[54] https://wfirst.gsfc.nasa.gov/
[55] This is determined by performing a crossmatch between BTS host positions and the SDSS imaging catalog. Any hosts with SDSS sources within 1′ are assumed to be within the SDSS imaging footprint.

of the BTS—classify all the bright transients—has resulted in the largest systematic classification of SNe to date. A total of 761 SNe are included in this early release paper, while the inclusion of 2019 results will eventually bring this number to >1800. In addition to measuring the RCF, as was done here, our growing sample can be used to determine volumetric SN rates, measure the expansion of the universe using low-z SNe Ia, study the demographics of CC SNe, and measure the luminosity function of a wide range of transient phenomena. This, despite the fact that BTS only targets a tiny minority of all transients discovered by ZTF. The BTS demonstrates that a focused triage of an otherwise overwhelming discovery stream can lead to both impactful and novel results.

Appendix
Measuring the Conditional Probability of the RCF

To estimate the conditional probability that a galaxy has a cataloged redshift based on its distance and IR luminosity, we model the data X with the Bernoulli distribution

$$X \sim \text{Bern}(p), \tag{A1}$$

where p is parameterized with a logistic function with dependence on both redshift z and host-galaxy luminosity:

$$p(z, M, \theta) = \frac{1}{1 + \exp(az + bM - c)}, \tag{A2}$$

with host-galaxy absolute magnitude M and θ representing the model parameters a, b, and c, which need to be determined.
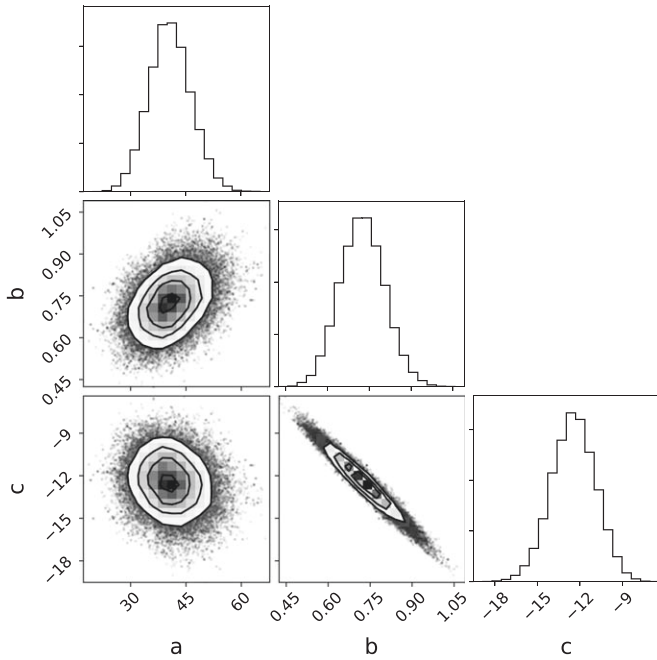
Figure A1. Corner plot showing the posterior distribution of a, b, and c, used to constrain the joint distribution of the RCF on z and M_{W_1}, RCF(z, M_{W_1}).

(The data used to create this figure are available.)

The precise analytic dependence of p on z and M may not be logistic; however, the purpose of this exercise is to provide a general sense for how the RCF relies on z and M. Given that it smoothly transitions over an exponential length scale from 1 to 0, the logistic function works well for this general purpose.

From here it follows that the probability of a host galaxy having a previously cataloged redshift is

$$Pr(q) = \begin{cases} p(z, M, \theta), & \text{if } q = \text{NED}_z \\ 1 - p(z, M, \theta), & \text{if } q =! \text{NED}_z \end{cases}, \quad (A3)$$

and the likelihood of the observations given the data and model parameters is

$$\begin{aligned} Pr(q_k \,|\, z_k, M_k, \theta) \\ = \textstyle\prod_{k=1}^{K} p(z_k, M_k, \theta)^{q_k} (1 - p(z_k, M_k, \theta)^{1-q_k}, \end{aligned} \quad (A4)$$

where k represents the individual observations and $q_k = 1$ for NED$_z$ galaxies and $q_k = 0$ for !NED$_z$ galaxies.

To estimate the model parameters, we adopt wide, flat priors and use the affine-invariant Markov Chain Monte Carlo (MCMC) ensemble sampling technique described by Goodman & Weare (2010), as implemented in the emcee software package (Foreman-Mackey et al. 2013) . For a and b, we adopt flat priors bounded between 0 and 10^6. For c, we adopt a flat prior between -100 and 100. We use 25 walkers within the sample and run the ensemble until it has "converged," which we define as >100 times longer than the average autocorrelation length of the individual chains from each walker. We find that there is a strong covariance between b and c, whereas a is relatively independent, as shown in the corner plot in Figure A1. The posterior samples are attached as data behind the figure.

We also constrain the RCF as a function of the host redshift, z, or host-galaxy luminosity, individually. We do this separately from the analysis above, while using the same MCMC procedure with p in Equations (A3) and (A4) replaced by

$$p(z, \theta) = \frac{1}{1 + \exp(az - c)} \quad (A5)$$

for redshift, and

$$p(M, \theta) = \frac{1}{1 + \exp(bM - c)} \quad (A6)$$

for host-galaxy luminosity (where, again, we use absolute magnitude M_{W1} instead of total luminosity). The results of this procedure are shown in the side panels of Figure 8. In these panels, the solid lines show the median value of $p(z)$, RCF(z), and $p(M)$, RCF(M), while the shaded region shows the 90% credible regions for $p(z)$ and $p(M)$.

ORCID iDs

C. Fremling ⓘ https://orcid.org/0000-0002-4223-103X
A. A. Miller ⓘ https://orcid.org/0000-0001-9515-478X
Y. Sharma ⓘ https://orcid.org/0000-0003-4531-1745
A. Dugas ⓘ https://orcid.org/0000-0001-7344-0208
D. A. Perley ⓘ https://orcid.org/0000-0001-8472-1996
K. Taggart ⓘ https://orcid.org/0000-0002-5748-4558
J. Sollerman ⓘ https://orcid.org/0000-0003-1546-6615
A. Goobar ⓘ https://orcid.org/0000-0002-4163-4996
M. L. Graham ⓘ https://orcid.org/0000-0002-9154-3136
J. D. Neill ⓘ https://orcid.org/0000-0002-0466-1119
M. Rigault ⓘ https://orcid.org/0000-0002-8121-2560
I. Andreoni ⓘ https://orcid.org/0000-0002-8977-1498
E. C. Bellm ⓘ https://orcid.org/0000-0001-8018-5348
S. B. Cenko ⓘ https://orcid.org/0000-0003-1673-970X
R. Dekany ⓘ https://orcid.org/0000-0002-5884-7867
S. Frederick ⓘ https://orcid.org/0000-0001-9676-730X
V. Z. Golkhou ⓘ https://orcid.org/0000-0001-8205-2506
M. J. Graham ⓘ https://orcid.org/0000-0002-3168-0139
A. Y. Q. Ho ⓘ https://orcid.org/0000-0002-9017-3567
M. M. Kasliwal ⓘ https://orcid.org/0000-0002-5619-4938
T. Kupfer ⓘ https://orcid.org/0000-0002-6540-1484
R. R. Laher ⓘ https://orcid.org/0000-0003-2451-5482
A. Mahabal ⓘ https://orcid.org/0000-0003-2242-0244
F. J. Masci ⓘ https://orcid.org/0000-0002-8532-9395
R. Riddle ⓘ https://orcid.org/0000-0002-0387-370X
B. Rusholme ⓘ https://orcid.org/0000-0001-7648-4142
S. Schulze ⓘ https://orcid.org/0000-0001-6797-1889
D. L. Shupe ⓘ https://orcid.org/0000-0003-4401-0430
R. M. Smith ⓘ https://orcid.org/0000-0001-7062-9726
S. van Velzen ⓘ https://orcid.org/0000-0002-3859-8074
Lin Yan ⓘ https://orcid.org/0000-0003-1710-9339
Y. Yao ⓘ https://orcid.org/0000-0001-6747-8509
S. R. Kulkarni ⓘ https://orcid.org/0000-0001-5390-8563

References

Abolfathi, B., Aguado, D. S., Aguilar, G., et al. 2018, ApJS, 235, 42
Aguado, D. S., Ahumada, R., Almeida, A., et al. 2019, ApJS, 240, 23
Aldering, G., Adam, G., Antilogus, P., et al. 2002, Proc. SPIE, 4836, 61
Andreoni, I., Goldstein, D. A., Anand, S., et al. 2019, ApJL, 881, L16
Angus, C. R., Smith, M., Sullivan, M., et al. 2019, MNRAS, 487, 2215

Arnett, W. D., Bahcall, J. N., Kirshner, R. P., & Woosley, S. E. 1989, ARA&A, 27, 629
Astier, P., Guy, J., Regnault, N., et al. 2006, A&A, 447, 31
Astropy Collaboration, Robitaille, T. P., Tollerud, E. J., et al. 2013, A&A, 558, A33
Baade, W., & Zwicky, F. 1934, PhRv, 46, 76
Bellm, E. C. 2016, PASP, 128, 084501
Bellm, E. C., Kulkarni, S. R., Barlow, T., et al. 2019a, PASP, 131, 068003
Bellm, E. C., Kulkarni, S. R., Graham, M. J., et al. 2019b, PASP, 131, 018002
Bellm, E. C., & Sesar, B. 2016, pyraf-dbsp: Reduction pipeline for the Palomar Double Beam Spectrograph, Astrophysics Source Code Library, ascl:1602.002
Ben-Ami, S., Konidaris, N., Quimby, R., et al. 2012, Proc. SPIE, 8446, 844686
Blagorodnova, N., Neill, J. D., Walters, R., et al. 2018, PASP, 130, 035003
Blondin, S., Dessart, L., & Hillier, D. J. 2015, MNRAS, 448, 2766
Blondin, S., & Tonry, J. L. 2007, in AIP Conf. Ser. 924, The Multicolored Landscape of Compact Objects and Their Explosive Origins, ed. T. di Salvo et al. (Melville, NY: AIP), 312
Branch, D., Dang, L. C., Hall, N., et al. 2006, PASP, 118, 560
Cenko, S. B., Fox, D. B., Moon, D.-S., et al. 2006, PASP, 118, 1396
Chambers, K. C., Magnier, E. A., Metcalfe, N., et al. 2016, arXiv:1612.05560
Cook, D. O., Kasliwal, M. M., Van Sistine, A., et al. 2019, ApJ, 880, 7
Cortini, G. 2018, TNSTR, 393, 1
Coughlin, M. W., Ahumada, T., Anand, S., et al. 2019, arXiv:1907.12645
Davenport, J., de Val-Borro, M., & Wilkinson, T. D. 2016, pydis: Possibly Useful, v1.1., Zenodo, doi:10.5281/zenodo.58753
De Cia, A., Gal-Yam, A., Rubin, A., et al. 2018, ApJ, 860, 100
Dekany, R., Smith, R. M., Riddle, R., et al. 2020, PASP, 132, 038001
DESI Collaboration, Aghamousa, A., Aguilar, J., et al. 2016, arXiv:1611.00036
Dey, A., Schlegel, D. J., Lang, D., et al. 2019, AJ, 157, 168
Duev, D. A., Mahabal, A., Masci, F. J., et al. 2019, arXiv:1907.11259
Filippenko, A. V. 1997, ARA&A, 35, 309
Filippenko, A. V., Li, W. D., Treffers, R. R., & Modjaz, M. 2001, in ASP Conf. Ser. 246, IAU Coll. 183: Small Telescope Astronomy on Global Scales, ed. B. Paczynski, W.-P. Chen, & C. Lemme (San Francisco, CA: ASP), 121
Fitzpatrick, E. L., & Massa, D. 2007, ApJ, 663, 320
Flesch, E. W. 2015, PASA, 32, e010
Foley, R. J., Li, W., Moore, M., et al. 2006, CBET, 695, 1
Foley, R. J., Smith, N., Ganeshalingam, M., et al. 2007, ApJL, 657, L105
Foreman-Mackey, D. 2016, JOSS, 1, 24
Foreman-Mackey, D., Hogg, D. W., Lang, D., & Goodman, J. 2013, PASP, 125, 306
Fox, O. D., Azalee Bostroem, K., Van Dyk, S. D., et al. 2014, ApJ, 790, 17
Frieman, J. A., Bassett, B., Becker, A., et al. 2008, AJ, 135, 338
Gaia Collaboration, Prusti, T., de Bruijne, J. H. J., et al. 2016, A&A, 595, A1
Galama, T. J., Vreeswijk, P. M., van Paradijs, J., et al. 1998, Natur, 395, 670
Gal-Yam, A. 2012, Sci, 337, 927
Gal-Yam, A., Mazzali, P., Ofek, E. O., et al. 2009, Natur, 462, 624
Gehrels, N., Cannizzo, J. K., Kanner, J., et al. 2016, ApJ, 820, 136
Goobar, A., & Leibundgut, B. 2011, ARNPS, 61, 251
Goodman, J., & Weare, J. 2010, CAMCS, 5, 65
Goodman, L. A. 1965, Technometrics, 7, 247
Gorbovskoy, E. S., Lipunov, V. M., Kornilov, V. G., et al. 2013, ARep, 57, 233
Graham, M. J., Kulkarni, S. R., Bellm, E. C., et al. 2019, PASP, 131, 078001
Grzegorzek, J. 2018, TNSTR, 582, 1
Gutiérrez, C. P., Anderson, J. P., Hamuy, M., et al. 2017, ApJ, 850, 89
Helfand, D. J., White, R. L., & Becker, R. H. 2015, ApJ, 801, 26
Hirata, K., Kajita, T., Koshiba, M., et al. 1987, PhRvL, 58, 1490
Ho, A. Y. Q., Phinney, E. S., Ravi, V., et al. 2019, ApJ, 871, 73
Hodgkin, S. T., Wyrzykowski, L., Blagorodnova, N., & Koposov, S. 2013, RSPTA, 371, 20120239
Holoien, T. W. S., Brown, J. S., Stanek, K. Z., et al. 2017a, MNRAS, 467, 1098
Holoien, T. W. S., Brown, J. S., Stanek, K. Z., et al. 2017b, MNRAS, 471, 4966
Holoien, T. W. S., Brown, J. S., Vallely, P. J., et al. 2019, MNRAS, 484, 1899
Holoien, T. W. S., Stanek, K. Z., Kochanek, C. S., et al. 2017c, MNRAS, 464, 2672
Howell, D. A. 2001, ApJL, 554, L193
Hunter, J. D. 2007, CSE, 9, 90
Itagaki, K. 2018a, TNSTR, 1614, 1
Itagaki, K. 2018b, TNSTR, 1766, 1
Ivezić, Ž., Tyson, J. A., Acosta, E., et al. 2008, arXiv:0805.2366

Jarrett, T. H., Cohen, M., Masci, F., et al. 2011, ApJ, 735, 112
Kasen, D. 2006, ApJ, 649, 939
Kasliwal, M. M., Cannella, C., Bagdasaryan, A., et al. 2019, PASP, 131, 038003
Kasliwal, M. M., Kulkarni, S. R., Gal-Yam, A., et al. 2012, ApJ, 755, 161
Kasliwal, M. M., & Nissanke, S. 2014, ApJL, 789, L5
Kulkarni, S. R., Perley, D. A., & Miller, A. A. 2018, ApJ, 860, 22
Lang, D., Hogg, D. W., & Mykytyn, D. 2016a, The Tractor: Probabilistic Astronomical Source Detection and Measurement, Astrophysics Source Code Library, ascl:1604.008
Lang, D., Hogg, D. W., & Schlegel, D. J. 2016b, AJ, 151, 36
Law, N. M., Kulkarni, S. R., Dekany, R. G., et al. 2009, PASP, 121, 1395
Li, W., Leaman, J., Chornock, R., et al. 2011, MNRAS, 412, 1441
Li, W. D., Filippenko, A. V., Treffers, R. R., et al. 2000, in AIP Conf. Ser. 522, Cosmic Explosions, ed. S. S. Holt & W. W. Zhang (Melville, NY: AIP), 103
Ligo Scientific Collaboration & VIRGO Collaboration 2019a, GCN, 24168, 1
Ligo Scientific Collaboration & VIRGO Collaboration 2019b, GCN, 24442, 1
Ligo Scientific Collaboration & VIRGO Collaboration 2019c, GCN, 25606, 1
Ligo Scientific Collaboration & VIRGO Collaboration 2019d, GCN, 25707, 1
Liu, Y.-Q., Modjaz, M., Bianco, F. B., & Graur, O. 2016, ApJ, 827, 90
Lunnan, R., Yan, L., Perley, D. A., et al. 2019, arXiv:1910.02968
Mahabal, A., Rebbapragada, U., Walters, R., et al. 2019, PASP, 131, 038002
Maraston, C., Pforr, J., Henriques, B. M., et al. 2013, MNRAS, 435, 2764
Martin, D. C., Fanson, J., Schiminovich, D., et al. 2005, ApJL, 619, L1
Masci, F. J., Laher, R. R., Rusholme, B., et al. 2019, PASP, 131, 018003
McCray, R. 1993, ARA&A, 31, 175
McKinney, W. 2010, in Proc. 9th Python in Science Conf., ed. S. van der Walt & J. Millman, 51
Modjaz, M., Blondin, S., Kirshner, R. P., et al. 2014, AJ, 147, 99
Modjaz, M., Liu, Y. Q., Bianco, F. B., & Graur, O. 2016, ApJ, 832, 108
Nordin, J., Brinnel, V., van Santen, J., et al. 2019, arXiv:1904.05922
Norgaard-Nielsen, H. U., Hansen, L., Jorgensen, H. E., Aragon Salamanca, A., & Ellis, R. S. 1989, Natur, 339, 523
Oke, J. B., Cohen, J. G., Carr, M., et al. 1995, PASP, 107, 375
Oke, J. B., & Gunn, J. E. 1982, PASP, 94, 586
Papadogiannakis, S., Dhawan, S., Morosin, R., & Goobar, A. 2019a, MNRAS, 485, 2343
Papadogiannakis, S., Goobar, A., Amanullah, R., et al. 2019b, MNRAS, 483, 5045
Pastorello, A., Smartt, S. J., Botticella, M. T., et al. 2010, ApJL, 724, L16
Pastorello, A., Smartt, S. J., Mattila, S., et al. 2007, Natur, 447, 829
Patat, F., Cappellaro, E., Danziger, J., et al. 2001, ApJ, 555, 900
Patterson, M. T., Bellm, E. C., Rusholme, B., et al. 2019, PASP, 131, 018001
Perley, D. A. 2019, PASP, 131, 084503
Perley, D. A., Mazzali, P. A., Yan, L., et al. 2019, MNRAS, 484, 1031
Perlmutter, S., Aldering, G., Goldhaber, G., et al. 1999, ApJ, 517, 565
Piascik, A. S., Steele, I. A., Bates, S. D., et al. 2014, Proc. SPIE, 9147, 91478H
Prentice, S. J., Maguire, K., Smartt, S. J., et al. 2018, ApJL, 865, L3
Quimby, R. M., Aldering, G., Wheeler, J. C., et al. 2007, ApJL, 668, L99
Quimby, R. M., De Cia, A., Gal-Yam, A., et al. 2018, ApJ, 855, 2
Quimby, R. M., Kulkarni, S. R., Kasliwal, M. M., et al. 2011, Natur, 474, 487
Riess, A. G., Filippenko, A. V., Challis, P., et al. 1998, AJ, 116, 1009
Rigault, M., Neill, J. D., Blagorodnova, N., et al. 2019, A&A, 627, A115
Schlafly, E. F., & Finkbeiner, D. P. 2011, ApJ, 737, 103
Schlafly, E. F., Meisner, A. M., & Green, G. M. 2019, ApJS, 240, 30
Schlegel, D. J., Finkbeiner, D. P., & Davis, M. 1998, ApJ, 500, 525
Schlegel, E. M. 1990, MNRAS, 244, 269
Schmidt, B. P., Kirshner, R. P., Eastman, R. G., et al. 1993, Natur, 364, 600
Science Software Branch at STScI 2012, PyRAF: Python alternative for IRAF, Astrophysics Source Code Library, ascl:1207.011
Secrest, N. J., Dudik, R. P., Dorland, B. N., et al. 2015, ApJS, 221, 12
Shappee, B., Prieto, J., Stanek, K. Z., et al. 2014, AAS Meeting Abstracts, 223, 236.03
Signorell, A., Aho, K., Alfons, A., et al. 2019, DescTools: Tools for Descriptive Statistics, https://cran.r-project.org/package=DescTools
Silverman, J. M., Foley, R. J., Filippenko, A. V., et al. 2012, MNRAS, 425, 1789
Smartt, S. J., Valenti, S., Fraser, M., et al. 2015, A&A, 579, A40
Smith, N., Li, W., Foley, R. J., et al. 2007, ApJ, 666, 1116
Soumagnac, M. T., & Ofek, E. O. 2018, PASP, 130, 075002
Sun, P., Lau, A., Liu, J., et al. 2018, TNSTR, 2007, 1
Tachibana, Y., & Miller, A. A. 2018, PASP, 130, 128001
Tanaka, Y. 2018, TNSTR, 469, 1
Tartaglia, L., Sand, D. J., Valenti, S., et al. 2018, ApJ, 853, 62

Taubenberger, S. 2017, in Handbook of Supernovae, ed. A. W. Alsabti & P. Murdin (Cham: Springer), 317

Tody, D. 1986, Proc. SPIE, 627, 733

Tonry, J. L., Denneau, L., Heinze, A. N., et al. 2018, PASP, 130, 064505

Turatto, M., Cappellaro, E., Danziger, I. J., et al. 1993, MNRAS, 262, 128

Virtanen, P., Gommers, R., Oliphant, T. E., et al. 2020, Nature Methods, 17, 261

Wen, X.-Q., Wu, H., Zhu, Y.-N., et al. 2013, MNRAS, 433, 2946

Williamson, M., Modjaz, M., & Bianco, F. B. 2019, ApJL, 880, L22

Wright, E. L., Eisenhardt, P. R. M., Mainzer, A. K., et al. 2010, AJ, 140, 1868

Yao, Y., Miller, A. A., Kulkarni, S. R., et al. 2019, ApJ, 886, 152

Zackay, B., Ofek, E. O., & Gal-Yam, A. 2016, ApJ, 830, 27

Zhang, M., Ding, Y., Liu, S., et al. 2018, TNSTR, 1393, 1

Zhang, T.-M., Wang, X.-F., Chen, J.-C., et al. 2015, RAA, 15, 215

Zwicky, F. 1938a, PASP, 50, 215

Zwicky, F. 1938b, ApJ, 88, 529

Zwicky, F. 1942, ApJ, 96, 28